# SOURCES OF ERROR IN THE PHOTOCLINOMETRIC DETERMINATION OF PLANETARY TOPOGRAPHY: A REAPPRAISAL

NICHOLAS D. EFFORD

*Environmental Science Division, Institute of Environmental and Biological Sciences, Lancaster University, Lancaster, England, U.K.*

(Received 21 February, 1991)

**Abstract.** The technique of photoclinometry has frequently been used to determine planetary topography without proper consideration of possible sources of error. Previous studies of error sources have been limited in extent and have overlooked the importance of factors such as atmospheric scattering and the choice of a surface photometric function. This paper adopts a thorough and more direct approach to error analysis, whereby known topography is compared with photoclinometric profiles derived from synthetic quantised reflectance scans.

Instrumental and geometric sources of error are found to exert a minimal influence on profiles in practice, provided that sufficient care is taken in the selection of images and the extraction of scans from those images. Environmental factors – relating to the scattering properties of the surface and, if present, atmosphere – are far more important. It is found that a simple Lommel–Seeliger law is unlikely to be appropriate to the majority of planetary terrains, given its inability to model the effects of multiple scattering or unresolved macroscopic roughness. It is further demonstrated that a Minnaert function or combination of Lommel–Seeliger and Lambert laws may empirically compensate for the first of these phenomena but not the second; in this respect, Hapke's equation is a far superior model of surface optical properties. In the case of an atmosphere, the need to correct for scattering by aerosols or suspended dust becomes more acute as atmospheric opacity increases and as particle scattering becomes more forward-biased. To perform this correction, a model for the combined reflectance of surface and atmosphere must be used when deriving profiles.

Two case studies – of a small impact crater on Triton and a dust-mantled basaltic lava flow on Mars – are presented here. Regarding the latter, the implications that errors in photoclinometric flow thickness measurements have for inferred lava rheology are examined. Conservative estimates of errors in yield strength and apparent viscosity easily exceed 100% when one of the simplest photometric models possible – a Lommel–Seeliger law – is used to derive a profile.

In the light of these findings, strategies are suggested for improving the results obtained from photoclinometry in the future.

## 1. Introduction

The two classic techniques commonly employed to extract topographic information from spacecraft imaging data – stereophotogrammetry and shadow length measurement – suffer from drawbacks that limit their applicability in many situations; the former is accurate but expensive computationally, and the construction of stereo pairs requires overlapping coverage of the target body's surface which is usually absent at high spatial resolutions; the latter is simple and requires only a single image, but its use is generally restricted to areas of rugged terrain reasonably close to the planetary terminator. Furthermore, shadow length calculations yield only the difference in elevation between points at the root and the foot of a

*Earth, Moon, and Planets* **54**: 19–58, 1991.

shadow, which will not necessarily correspond to a meaningful topographic measure such as crater depth.

Photoclinometry is a technique applicable in a much wider range of situations. It utilises single images in which resolvable shadowing is minimal or absent and in principle it is capable of determining surface topography in one or two lateral dimensions. In general, the mapping of topography over an area is a problem more complex than that of extracting a topographic profile. The sophisticated 'shape from shading' algorithms so far applied to well-constrained problems in the field of robot vision show some promise in planetary mapping applications (Van Hove and Carlotto, 1986), but most uses of photoclinometry to date have concentrated on taking single or multiple cross-sections through features of interest on a planetary surface; this paper therefore deals solely with the errors likely to accrue when individual profiles are derived from spacecraft images.

## 2. Practical Basis of Photoclinometry

In essence, topography is determined by modelling the influence of tilt relative to some reference surface on the measured reflectance of pixels in an image – or, in practice, on the ratio, $R$, of measured reflectance to that of a locally flat surface element, identically viewed and illuminated. One may write

$$R = \frac{r(i - \gamma, e - \gamma, g)}{r^*(i, e, g)}, \tag{1}$$

where $g$ is the phase angle, $i$ and $e$ are incidence and emergence angles measured relative to the flat surface element and $\gamma$ is the local surface tilt (see Figure 1). $r$ and $r^*$ are the reflectances of the tilted and flat surface elements, respectively; the two quantities are distinguished by the fact that $r$ is measured from the image, whereas $r^*$ must be estimated or theoretically calculated.

Since surface tilt is the principal unknown quantity, the problem is one of inverting equation 1 so as to express $\gamma$ as a function of $R$. If this is to be achieved, a mathematical expression must be supplied for surface reflectance. Two basic forms of photometric model have commonly been used for this purpose. One of these, Minnaert's law (Minnaert, 1941), takes the form

$$r(\mu_0, \mu) = A\mu_0^k \mu^{k-1}. \tag{2}$$

The other, informally described as 'lunar-like' but referred to here as a Hapke–Irvine scattering law (cf. Noland and Veverka, 1977), can be written as

$$r(\mu_0, \mu, g) = A \frac{\mu_0}{\mu_0 + \mu} f(g). \tag{3}$$

In both equations, $\mu_0$ and $\mu$ are the cosines of $i$ and $e$, respectively. Although the parameters $A$ and $k$ in Equation (2) are strictly functions of $g$, they will usually

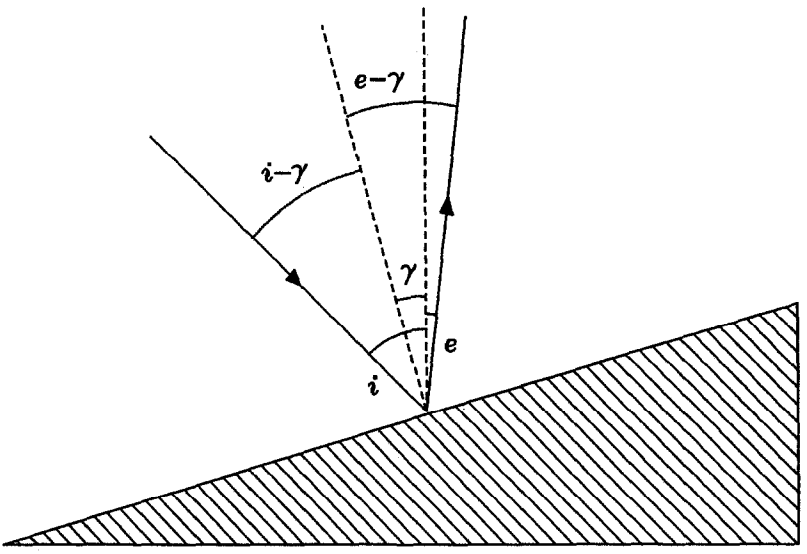


Fig. 1. Viewing and illumination geometry of a tilted surface for the simplest case where the incident light ray, emergent light ray and local surface normal are coplanar.

assume constant values within a single spacecraft image. In Equation (3), $f(g)$ is nomalised such that $f(0°) = 1$ and the constant $A$ is equal to twice the normal albedo of the surface at the point under study. Whether $f(g)$ is empirical or theoretical in form, its value is usually constant in a single image; Equation (3) thus reduces to a simple Lommel–Seeliger scattering law (Minnaert, 1961).

Equations (2) and (3) are simple, semi-empirical formulae which do not adequately describe the full range of phenomena involved in the scattering of light from a planetary surface. Hapke's equation for the reflectance of a rough-surfaced regolith (Hapke, 1981, 1984, 1986) is a more sophisticated, physically-parameterised model. It may be written as

$$r(\mu_0', \mu', g) = \frac{w}{4} \frac{\mu_0'}{\mu_0' + \mu'} \{[1 + B(g)]P(g) + H(\mu_0')H(\mu') - 1\} \times \quad (4)$$

$$\times S(\mu_0', \mu', g)\,,$$

where $w$ is the average single-scattering albedo of regolith particles; $B(g)$, models of the opposition effect (Hapke, 1986); and $P(g)$ describes the angular scattering characteristics of an average particle. Because both $B(g)$ and $P(g)$ are functions of phase angle alone, they become constants in most photoclinometric problems; the absolute values of the parameters controlling the influence of each on reflectance are thus relatively unimportant. The '$H$-functions' account for the effects of multiple scattering within the regolith (Hapke, 1981) and hence are dependent on $w$. $\mu_0'$ and $\mu'$ differ from $\mu_0$ and $\mu$, having been corrected for the effects of *unresolved* macroscopic roughness, and $S(\mu_0', \mu', g)$ is a function modelling the

shadowing caused by this roughness, which is assumed to have a mean slope angle $\bar{\theta}$ (Hapke, 1984).

In practice, photoclinometry begins with the extraction of a linear reflectance scan from an image, a task for which facilities are often provided by image processing systems. Once flat surface reflectance has been specified for each pixel along the scan, Equation (1) may be used to calculate reflectance ratios. The substitution of Equation (3) into Equation (1) leads to an analytic solution for $\gamma(R)$ (e.g., Jantunen and Raitala, 1983) which may be used to compute the tilt of each pixel-projected area of the surface along the scan. However, this is not possible if Equations (2) or (4) are used as photometric models; here, tilt is best determined by an iterative procedure, or by the initial generation of a tilt-reflectance ratio look-up table which may be rapidly accessed during profiling to obtain tilt estimates for each pixel along the scan. The final stage of the procedure involves the integration of tilts into elevations relative to the start of the profile, which is possible provided that the spatial resolution of the image is known.

## 3. Previous Work

Minnaert's law has featured in the application of photoclinometry to VIKING images of Mars (Howard *et al.*, 1982; Pike and Davis, 1984; Davis and Soderblom, 1984; Tanaka and Davis, 1988; Moore and Davis, 1990) and to VOYAGER images of Io (Moore *et al.*, 1986) and the uranian satellites (Jankowski and Squyres, 1988). The Lommel-Seeliger law has proved equally popular, having been applied to Mars (Jantunen and Raitala, 1983), the Jovian satellites Io (Davies and Wilson, 1987) and Ganymede (Squyres, 1981) and Saturn's moon Enceladus (Passey, 1983). It has also been linearly combined with a Lambert scattering law (Equation (2) with $k = 1$) in studies of Mars (McEwen, 1985) and various icy satellites (Schenk, 1989), motivated no doubt by the fact that such a combination appears to provide a better fit to observations of high albedo surfaces than either model alone (Buratti, 1984). Various forms of Hapke's equation have been used in photoclinometric studies of Mercury (Mouginis-Mark and Wilson, 1981) and of terrestrial surfaces (Wilson *et al.*, 1985, 1988) but few other investigations to date have utilised this model, despite the superior description of surface optical properties that it provides.

Studies dealing explicitly with sources of error in photoclinometry have been less numerous than those in which the technique has been applied. A rudimentary analysis by Davis and McEwen (1984) found photoclinometry to be a more robust technique at higher phase angles, where its sensitivity to variations or errors in viewing and illumination geometry, albedo, radiometric calibration and assumed photometric parameters is minimised. A subsequent study by Jankowski and Squyres (1990) has made use of an exhaustive list of possible error sources, incorporated here into Table I. They have mapped the net slope error arising from these sources for the specific cases of VIKING and VOYAGER images of

TABLE I

Possible sources of error in photoclinometry

| Type of error | Nature of error |
|---|---|
| Instrumental | Digitisation |
| | Pixel noise |
| | Background (dark current) |
| | Calibration |
| Geometric | Scanline misalignment |
| | Erroneous photometric geometry |
| Environmental | Unknown flat reflectance |
| | Surface albedo variations |
| | Invalid photometric function |
| | Atmospheric scattering |

Mars and Ganymede, respectively, and conclude that slope errors associated with digitisation and incorrect dark current removal are negligible in comparison with those that may be caused by image noise. They further find the influence of the variables in Table I to be enhanced near to the sub-solar point, and they confirm Davis and McEwen's (1984) observation on phase angle sensitivity; optimal conditions for photoclinometry of $g \approx 60°$ are cited, smaller phase angles resulting in larger slope errors and larger phase angles leading to geometric foreshortening the problems of which have been discussed by Davis and Soderblom (1984).

Howard *et al.* (1982) assessed the reliability of photoclinometric profiles derived from VIKING images of the martian north polar cap. They found that slopes estimated by the use of a Minnaert function became steeper as atmospheric opacity increased, although effects were negligible for optical depths less than 0.1. Errors were also found to increase dramatically as the angle between the illumination direction and the strike of the slopes neared zero. For the case of near-lambertian surface scattering (considered a reasonable approximation for snow or ice surfaces), variations of up to $\pm 30\%$ in the value assumed for Minnaert exponent $k$ were found to have only a small influence on estimated slopes. In contrast, the misestimation of flat surface reflectance or the neglect of albedo variations along a scan affected the results dramatically, proving to be capable of reversing the sense of the estimated slopes.

The implications of applying Hapke's equation in place of a Lommel–Seeliger law to VOYAGER images of terrain on Ganymede were examined in a cursory fashion by Wilson *et al.* (1983), who noted that the inclusion of sub-pixel scale roughness resulted in differences of up to 15% in the relative elevations derived using the two models. The results of that study must be considered to be very situation-specific, since real data were used and no attempt was made to consider the influence of each of the various error sources in isolation. To the author's knowledge, no other photoclinometric sensitivity analyses involving Hapke's equation have been published.

## 4. Aims and Approach

The error analyses discussed in Section 3 are of some value in that they provide guidelines helpful in the selection of suitable images and the extraction of reflectance scans from those images; however, none give a particularly clear or graphic indication of the resulting errors in the derived topography, or the corresponding implications that such errors may have. In some cases, it proves misleading to deal solely with slopes; for instance, Jankowski and Squyres (1990) quote errors owing to image noise of 2° near the sub-spacecraft point in Viking images, yet the presumably random nature of the noise spikes affecting images implies that there will be roughly as many positive slope errors as negative ones. This suggests in turn that the accumulated error in height will be relatively small. In contrast, the systematic error that results from flat surface reflectance misestimation leads to a consistent bias in estimated slopes and a concomitant large error in relative elevation at the end of a profile.

The length of a reflectance scan is obviously an important factor in determining the errors in photoclinometrically-derived topography; the longer the scan, the greater the error that accumulates. However, one should not assume proportionality between accumulated error and scan length; slope errors may vary greatly along a scan, being dependent on the magnitudes of the slopes themselves, on local viewing and illumination geometry and perhaps also on the optical properties of the terrain sampled along the scan.

Bearing in mind these factors, an approach to sensitivity analysis in which profiles are directly compared with known topography is potentially of great value. Such an approach is adopted in this paper to illustrate the results of some of the errors whose sources are listed in Table I. Emphasis has been placed on two of these error sources – relating to the choice of a photometric model and the presence of an atmosphere – because their importance has hitherto been only poorly appreciated. For example, Howard *et al.* (1982) stated of photoclinometry that

> . . . the technique is rather forgiving of errors in parameters of the photometric function . . .

which presupposes that Minnaert's law properly describes photometric behaviour. However, this proves to be the case only at low phase angles (Veverka *et al.*, 1986), where photoclinometry happens to be most sensitive to errors in other variables (Davis and McEwen, 1984; Jankowski and Squyres, 1990). Evidence is accumulating that Hapke's equation provides a far more appropriate description of scattering by a planetary regolith at visible wavelengths (Hapke, 1981, 1984, 1986; Simonelli and Veverka, 1986; Helfenstein and Veverka, 1987; Thomas *et al.*, 1987). Hence the basic assumption of this study has been that Hapke's model (Equation (4)) is the correct one and the consequences of adopting other, simpler scattering laws (e.g., Equations (2, 3)) have been explored.

TABLE II

Parameters defining a digitised cross-section through a hypothetical impact crater

| Parameter | Description | Value (m) |
|---|---|---|
| $d$ | Crater depth | 10 |
| $r_c$ | Crater radius | 40 |
| $h$ | Rim height | 1 |
| $r_m$ | Rim-merge radius | 55 |
| $\Delta x$ | Pixel size | 1.238 |

### 4.1 Generation of synthetic topography

Synthetic cross-sections through two planetary landforms were generated for use in these investigations. The first was a simple, bowl-shaped impact crater with a raised rim. Equations describing how elevation varies with radius for such a feature have been derived by Helfenstein (1986). For distances from the crater's centre less than its radius, $r_c$, one may write

$$z(x) = d\left[\left(\frac{x}{r_c}\right)^2 - 1\right] + h\,, \tag{5}$$

where $d$ is the rim-to-floor crater depth and $h$ is the rim height. Outside the crater, topography is assumed to decay with increasing distance according to an inverse-cube law. Thus

$$z(x) = \frac{h}{1 - (r_c/r_m)^3}\left[\left(\frac{r_c}{|x|}\right)^3 - 1\right] + h\,, \tag{6}$$

where $r_m$ is the radius at which rim topography merges with that of the surroundings. Table II gives values for the morphological parameters of the crater used in this study, and Figure 2 plots a cross-section through it.

A lava flow was used as a second landform. A Bingham plastic rheology was assumed, allowing Hulme's (1974) model to be employed. The equation used by Hulme to describe flow morphology in cross-section was modified slightly to make the levees visibly distinct from the flow's central channel. Hence

$$z(x) = \begin{cases} z_B(x) - \delta z & 0 < |x| \leqslant W_c/2\,, \\ z_B(x) & W_c/2 < |x| \leqslant W/2\,, \end{cases} \tag{7}$$

where

$$z_B(x) = \left[\frac{S_y(W - 2|x|)}{\rho g}\right]^{1/2}. \tag{8}$$

In Equations (7) and (8), $W_c$ and $W$ are the width of the channel and total width of the flow, respectively, $\rho$ is the density of the lava, $S_y$ is its yield strength and $g$

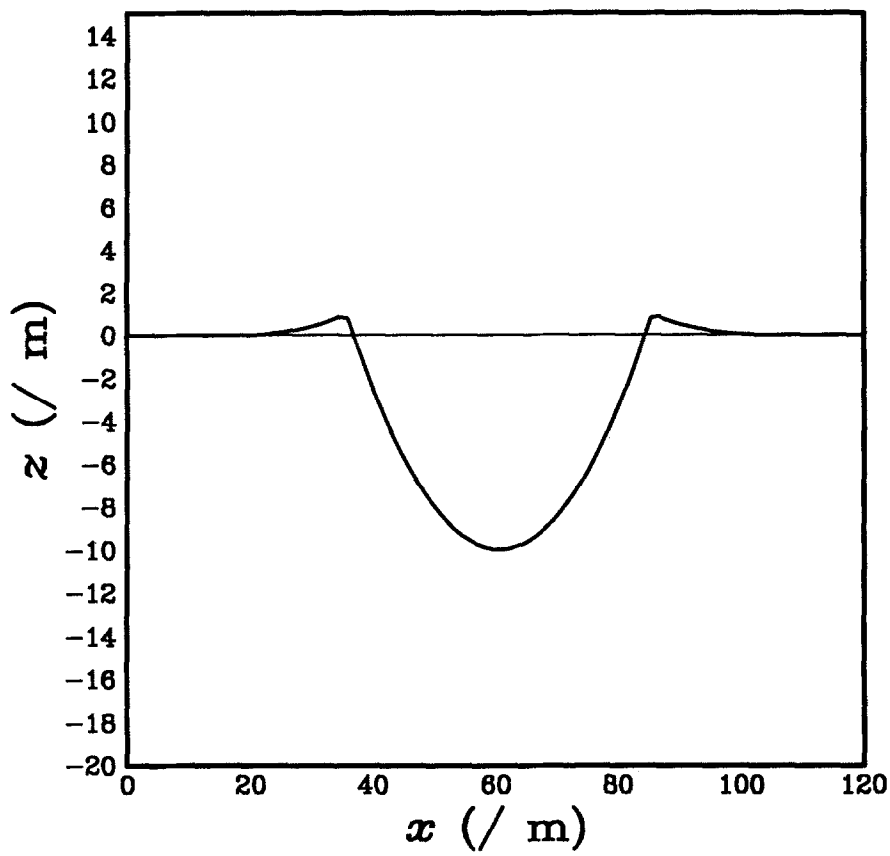


Fig. 2. Cross-section through the centre of the hypothetical impact crater used in this study.

is the local acceleration due to gravity. Table III gives the values adopted for these parameters; the widths are those measured by Moore and Davis (1990) for a flow on Ascraeus Mons, Mars; the lava density and yield strength used here are reasonable for Hawaiian basalts; the acceleration due to gravity at the Martian equator was assumed. Figure 3 plots the flow in cross-section.

### 4.2. Reflectance scan generation

For the simplest modelling described in Section 5, a Lommel–Seeliger law was used with $i = 40°$ and $e = 0°$ to generate reflectance scans from synthetic crater topography. More sophisticated exercises, in which the influence of surface scattering properties was examined, utilized Hapke's equation with an identical viewing and illumination geometry and the same topography. Here scans were generated using Equation (4) for surfaces which are: dark and smooth (DS); dark and rough (DR); bright and smooth (BS); bright and rough (BR). The Hapke parameters assumed for each of these terrain classes are listed in Table IV.

TABLE III

Parameters defining a digitised cross-section through a hypothetical lava flow having a Bingham rheology

| Parameter | Description | Value |
|---|---|---|
| $W$ | Flow width | 1340 m |
| $W_c$ | Channel width | 830 m |
| $\rho$ | Density | $2.6 \times 10^3$ kg m$^{-3}$ |
| $S_y$ | Yield strength | $3 \times 10^3$ Pa |
| $g$ | Gravity | 3.7 m s$^{-2}$ |
| $\Delta x$ | Pixel size | 20 m |

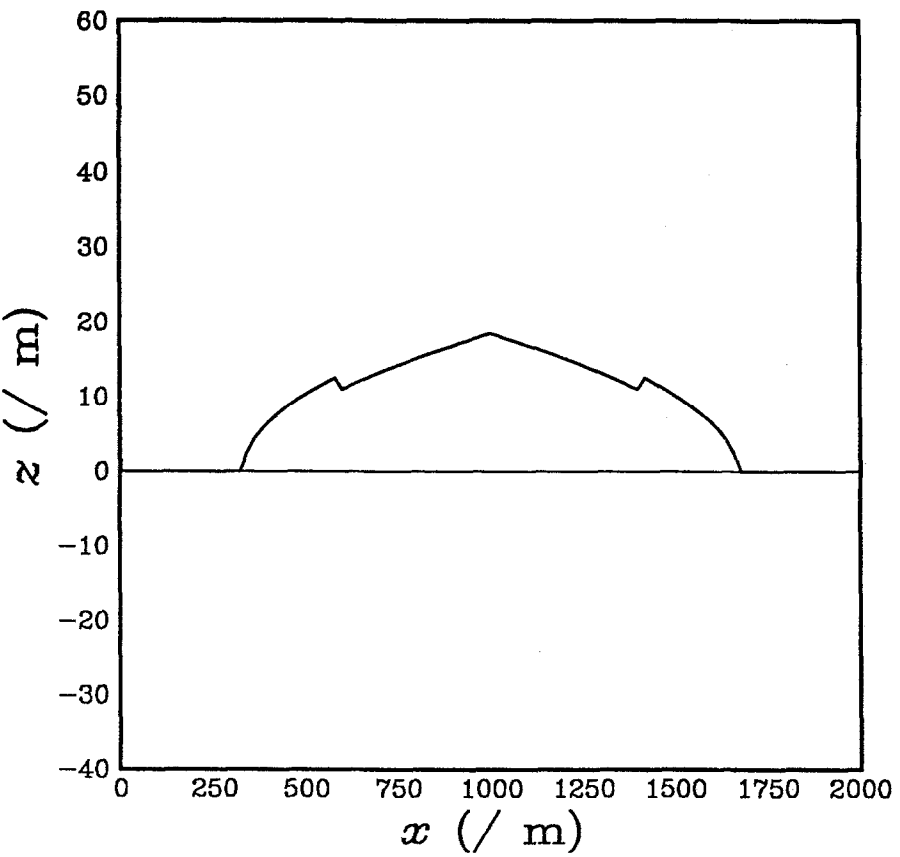


Fig. 3. Cross-section through the hypothetical lava flow used in this study. The topography expected for a Bingham plastic has been modified slightly to make the central channel distinct from the levees.

TABLE IV

Hapke parameters of model terrains used in this study. $b$ and $c$, coefficients of a second-order Legendre polynomial representing $P(g)$, remain constant; $B_0$ and $h$, parameters defining the amplitude and width of the opposition effect, are also fixed

| Terrain type | Hapke parameter | | | | | |
|---|---|---|---|---|---|---|
| | $w$ | $b$ | $c$ | $B_0$ | $h$ | $\bar{\theta}$ |
| DS | 0.1 | 0.3 | 0.4 | 1.5 | 0.09 | 0° |
| DR | 0.1 | · | · | · | · | 20° |
| BS | 0.95 | · | · | · | · | 0° |
| BR | 0.95 | · | · | · | · | 20° |

The modelling of atmospheric effects made use of a simple single-scattering approximation (Lumme *et al.*, 1981)

$$r = r_s e^{-\tau m} + r_a(1 - e^{-\tau m}) , \tag{9}$$

where $r_s$ and $r_a$ are the contributions of surface and atmosphere, respectively, to reflectance, $\tau$ is the optical depth and $m$, the air mass, is given by

$$m = \left(\frac{1}{\mu_0} + \frac{1}{\mu}\right)^{-1} . \tag{10}$$

For the atmospheric component a Hapke–Irvine law was assumed

$$r_a = \frac{w_a}{4} \frac{\mu_0}{\mu_0 + \mu} P_{HG}(g) , \tag{11}$$

where $w_a$ and $P_{HG}(g)$ are the average albedo and Henyey–Greenstein particle phase function of atmospheric scatterers. The cosines of $i$ and $e$ featuring in Equations (10) and (11) are distinct from those found in any expression for $r_s$; the former are calculated from the regional incidence and emergence angles; the latter are local in nature, $i$ and $e$ having been modified by surface tilt. The surface contribution to reflectance was described using Hapke's equation, with parameters appropriate to 'dark and smooth' terrain. Once again, crater topography with $i = 40°$ and $e = 0°$ was assumed.

A case study conducted using the crater topography of Figure 2 attempted to simulate conditions on Neptune's satellite Triton. Hillier *et al.* (1990) have determined photometric parameters appropriate to its surface and to atmospheric haze from the disk-integrated photometry of Voyager 2 data: their results are reproduced in Table V. $\bar{\theta}$ is taken here to be 10°, an average of the values estimated by Hillier *et al.* (1990) from green, blue and violet filter data, because no genuine wavelength dependence of photometric roughness is expected. The parameters of

TABLE V

Photometric parameters describing the surface and atmosphere of Triton as viewed through Voyager 2's green filter (effective wavelength 0.561 $\mu$m)

| Parameter | | Description | Value |
|---|---|---|---|
| Surface | $w$ | Single-scattering albedo | 0.996 |
| | $\epsilon_s$ | Asymmetry factor | −0.309 |
| | $\bar{\theta}$ | Photometric roughness | 10° |
| Atmosphere | $\epsilon_a$ | Asymmetry factor | 0.65 |
| | $\tau$ | Optimal depth | 0.03 |

TABLE VI

Photometric parameters describing the Martian surface and atmosphere. The former apply to the green channel of Viking Lander images, which spans a wavelength range of 0.5–0.59 $\mu$m

| Parameter | | Description | Value |
|---|---|---|---|
| Surface | $w_s$ | Single-scattering albedo | 0.48 |
| | $\epsilon_s$ | Asymmetry factor | −0.09 |
| | $S(0)$ | Opposition effect amplitude | 0.6 |
| | $h$ | Opposition effect width | 0.13 |
| Atmosphere | $w_a$ | Single-scattering albedo | 0.8 |
| | $\epsilon_a$ | Asymmetry factor | 0.5 |
| | $\tau$ | Optimal depth | 0.15 |

Table V were used to generate a synthetic reflectance scan at an incidence angle of 40°.

In a second case study, of a Martian lava flow, the atmosphere and surface parameters of Table VI were used; the former are reasonable for clear atmospheric conditions on Mars (Lumme *et al.*, 1981), whilst the latter are appropriate to dust deposits at the Viking Lander 1 site (Arvidson *et al.*, 1989). Unfortunately, no 'ground-truth' information exists on the surface texture of Martian lava flows, making the selection of an appropriate photometric roughness difficult. Airborne observations of terrestrial volcanic terrain (Guinness *et al.*, 1990) have suggested that photometric roughnesses as high as 40° might characterise surfaces composed of basalt fragments ranging from 1 cm to several tens of cm in size. However, flow surfaces on Mars are subject to the potential smoothing effects of aeolian weathering and dust deposition. Bearing in mind these factors, $\bar{\theta}$ for the flow surface was conservatively estimated at 20°. An incidence angle of 50° was used in generating scans across this feature.

Reflectances computed by the above methods were scaled into an 8-bit integer range to simulate the type of scan that would be extracted from digital images. 'DN', an acronym for *data number*, is used throughout this paper as a singular and plural term for these integer reflectances. Figure 4 shows scans derived from synthetic crater topography for each of the four generic terrain types modelled

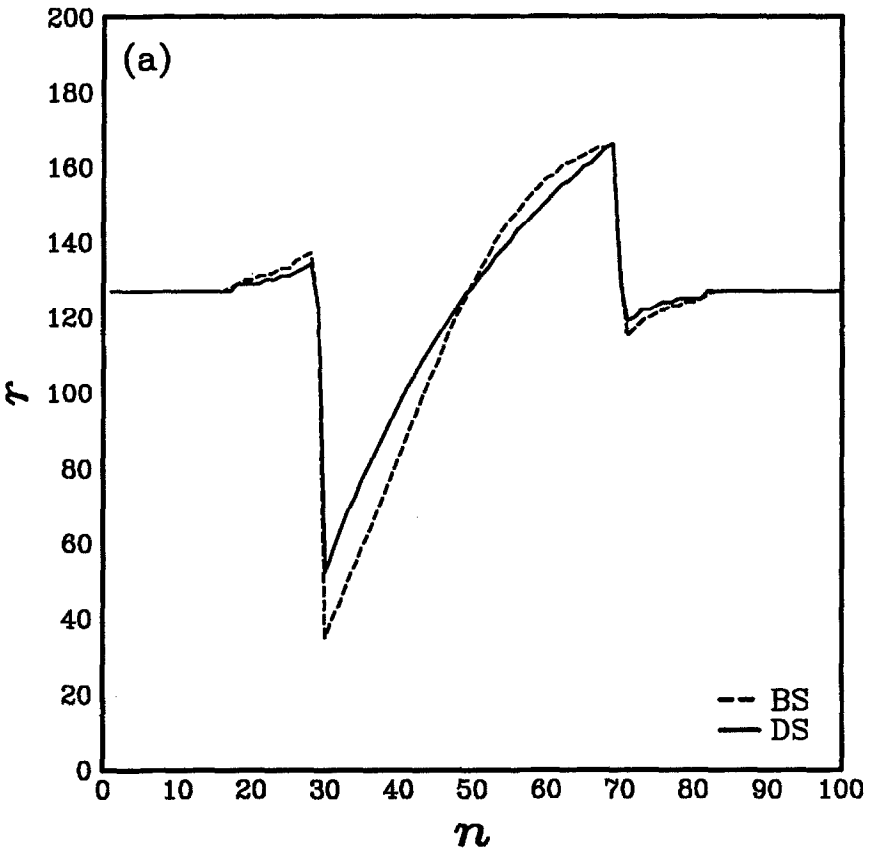


Fig. 4. Synthetic quantised reflectance scans across the crater of Figure 2, derived using Hapke's equation. Figure a illustrates the effects of multiple scattering within the regolith by comparing scans for dark ($w = 0.1$) and bright ($w = 0.95$) terrain; Figure b illustrates roughness effects by comparing scans for smooth ($\bar{\theta} = 0°$) and rough ($\bar{\theta} = 20°$) surfaces.

using Hapke's equation; (4a) illustrates the effects of particle albedo; (4b) illustrates the effects of unresolved macroscopic roughness. In each case, scans have been scaled to a common flat surface reflectance.

### 4.3. Topographic profiling

Topographic profiles were derived from reflectance scans using either a Minnaert function or a combination of Lommel–Seeliger and Lambert scattering laws: i.e.,

$$r(\mu_0, \mu) = A \frac{\mu_0}{\mu_0 + \mu} + (1 - A)\mu_0 , \tag{12}$$

where $A$ is a partitioning coefficient. In the latter case, tilts could be obtained analytically for $A = 1$, corresponding to pure Lommel–Seeliger behaviour; for other values of $A$, or for a Minnaert function, they were estimated by interpolation on a tilt-reflectance ratio look-up table. Figure 5 graphs the relationship between

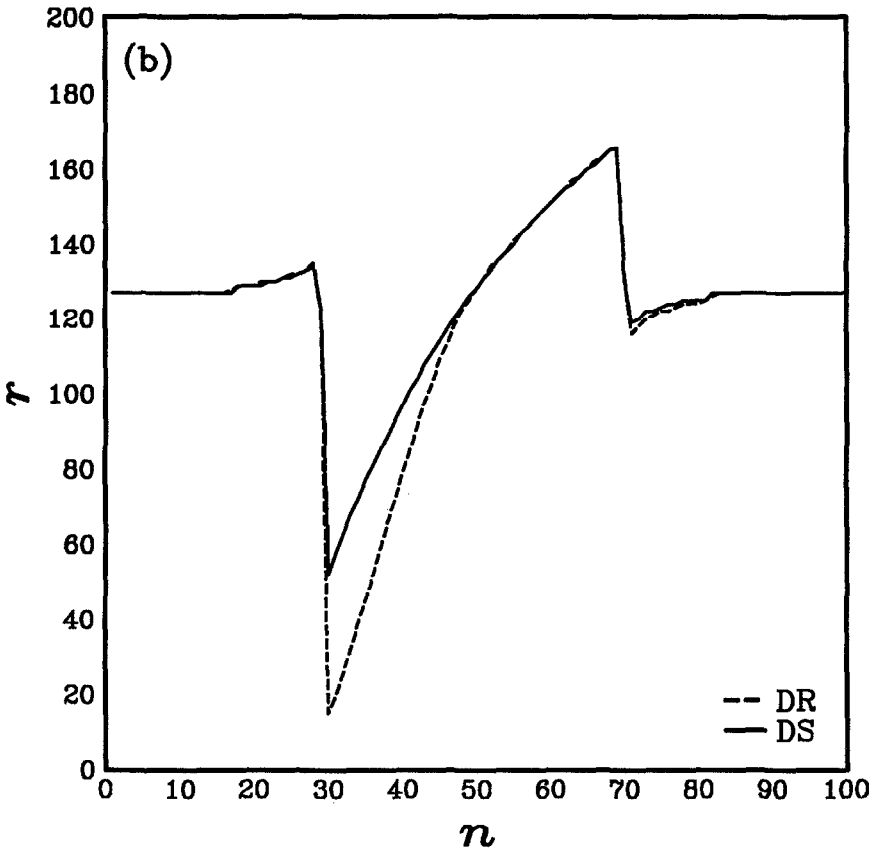


Fig. 4(b).

$\gamma$ and $R$ for a Minnaert function with various values of $k$; Figure 6 plots similar curves for Equation (12) with various partitioning coefficients.

## 5. Results

### 5.1. Instrumental factors

Figure 7 illustrates the effects on topography of a background reflectance level, found, for example, in vidicon images containing a residual dark current. To simulate the effects of such a background, a constant was added to the DN of reflectance scans generated from crater topography using Equation (3), prior to profiling using that same scattering law. The error in crater depth that arises is around 10% for the cases where the background amounts to 16% of the flat surface reflectance.

One instrumental factor not considered by Jankowski and Squyres (1990) is the linearity or otherwise of the relationship between the DN measured at an imaging pixel and the actual reflectance of the pixel-projected area on the target body's

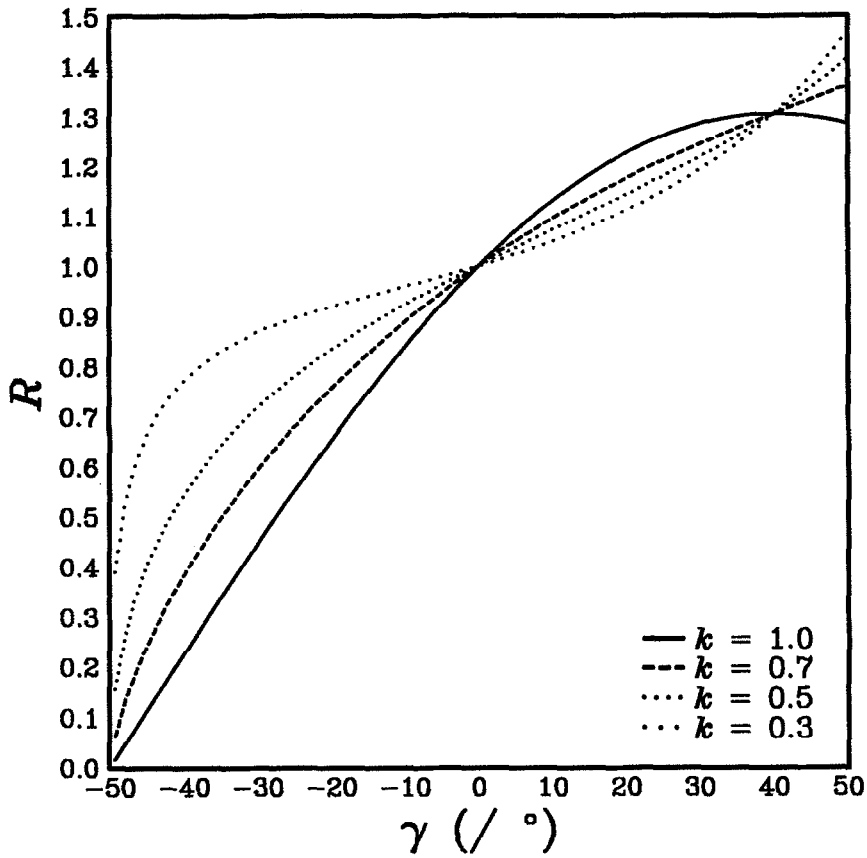


Fig. 5. The tilt-reflectance ratio look-up table of a Minnaert function, plotted for various values of the exponent $k$. $k = 1.0$ corresponds to Lambert's law.

surface. This is related to the question of a residual background by the fact that standard image calibration procedures are designed to remove dark current *and* correct for the possible non-linear light transfer characteristics of the sensor.

Non-linearity may arise if the image is uncalibrated or incorrectly calibrated, or if it has inadvertently undergone some form of non-linear contrast enhancement. The effect of these possibilities was investigated by contrast-stretching a reflectance scan using a variety of look-up tables, three of which (logarithmic, square root and quadratic) are shown in Figure 8. Figure 9 compares the profiles recovered from the stretched scans with the original topography. The greatest distortions occur for the quadratically-stretched scan because the stretch enhances reflectance variations at the high end of the scale, leading to gross overestimation of slopes on the bright, sunward-facing side of the crater. In the case of the square root stretch, a slight adjustment to assumed flat surface reflectance, $r^*$, levels the crater's rim crests (see Sections 5.3 and 6.3) but leads to a 50% underestimate of crater depth. For the quadratic stretch, a significant increase in $r^*$ is required to

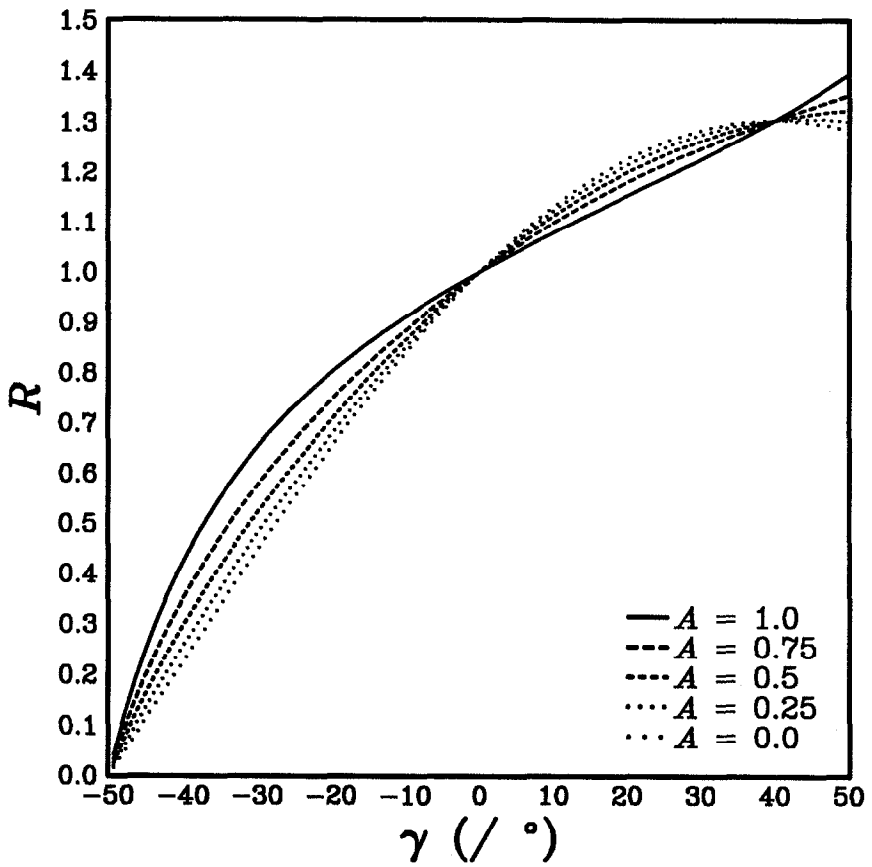


Fig. 6. The tilt-reflectance ratio look-up table of an empirical linear combination of Lommel–Seeliger and Lambert scattering laws, plotted for various values of the partitioning coefficient, $A$. When $A = 0$, scattering is purely lambertian in nature; when $A = 1$, the Lommel–Seeliger law is obeyed.

level the crater, but in the process depth is overestimated by 70% and the crater itself becomes asymmetrical in shape.

### 5.2. Geometric factors

A normal or near-normal viewing geometry (i.e., $e \approx 0°$) is desirable in photoclinometric problems since it minimises foreshortening and best facilitates the alignment of parallel reflectance scans. The emergence angle was therefore fixed at zero and the effects of errors in $i$ alone were investigated. A scan was generated using Equation (3) for an incidence angle of 40° and crater topography was photoclinometrically recovered from it, using a Lommel–Seeliger law but erroneously assuming incidence angles of 30° and 50°, respectively. Figure 10 depicts the results: where $i = 30°$ was assumed, the tilts of sloping regions are overestimated, leading to a error in crater depth of roughly +50%; where $i = 50°$ was assumed, the tilts of sloping regions are underestimated, leading to a crater depth error of

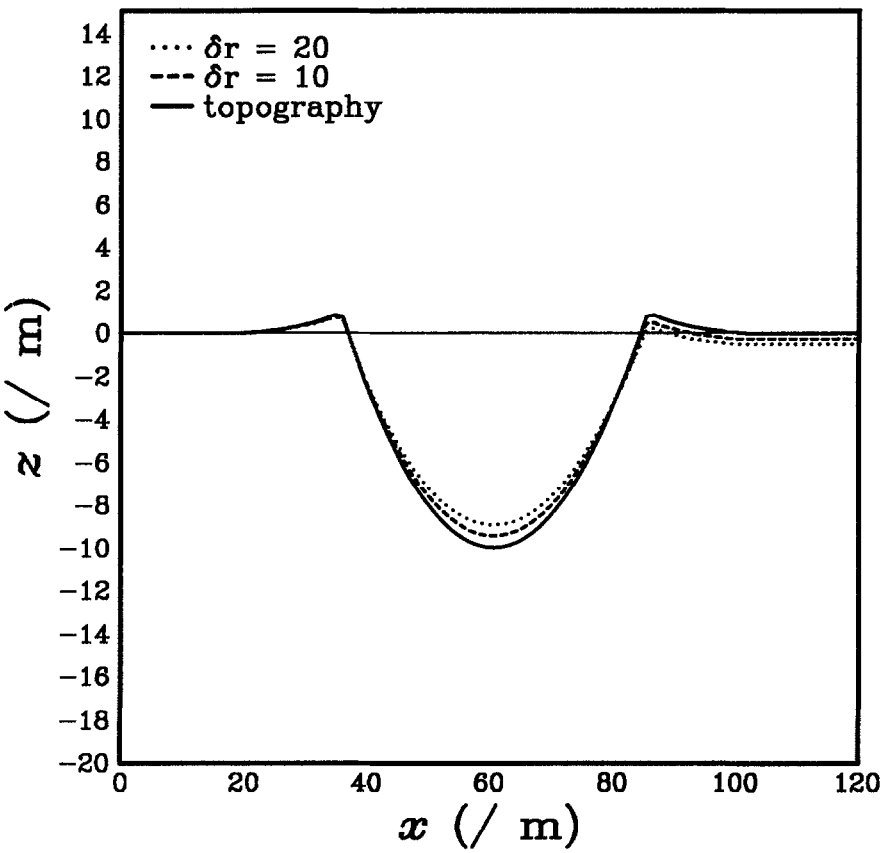


Fig. 7. The effect of a background level (residual dark current) on photoclinometric profiles of the crater in Figure 2. Curves are shown for levels, $\delta r$, of 10 and 20 DN, corresponding to 8% and 16% of the flat surface reflectance.

approximately −30%. These errors arise because $R$ becomes a steeper function of $\gamma$ as incidence angle increases from 30° to 50°.

### 5.3. Environmental Factors

#### 5.3.1. *Flat Surface Reflectance*

Evidently, the underestimation of flat surface reflectance will bias the reflectance ratios of Equation (1) toward larger values, thereby imparting to a profile a regional tilt toward the direction of illumination. The converse will apply when $r^*$ is overestimated. These effects are illustrated by Figure 11, which plots profiles derived with ±5% errors in the assumed reflectance of flat terrain. If a reflectance scan crosses several terrain units, concomittant albedo variations may make it necessary to assign a unique flat surface reflectance to each unit; failure to do this may impart a local tilt to short sections of the profile, affecting it in a manner more subtle than that illustrated in Figure 11. To demonstrate this, a reflectance

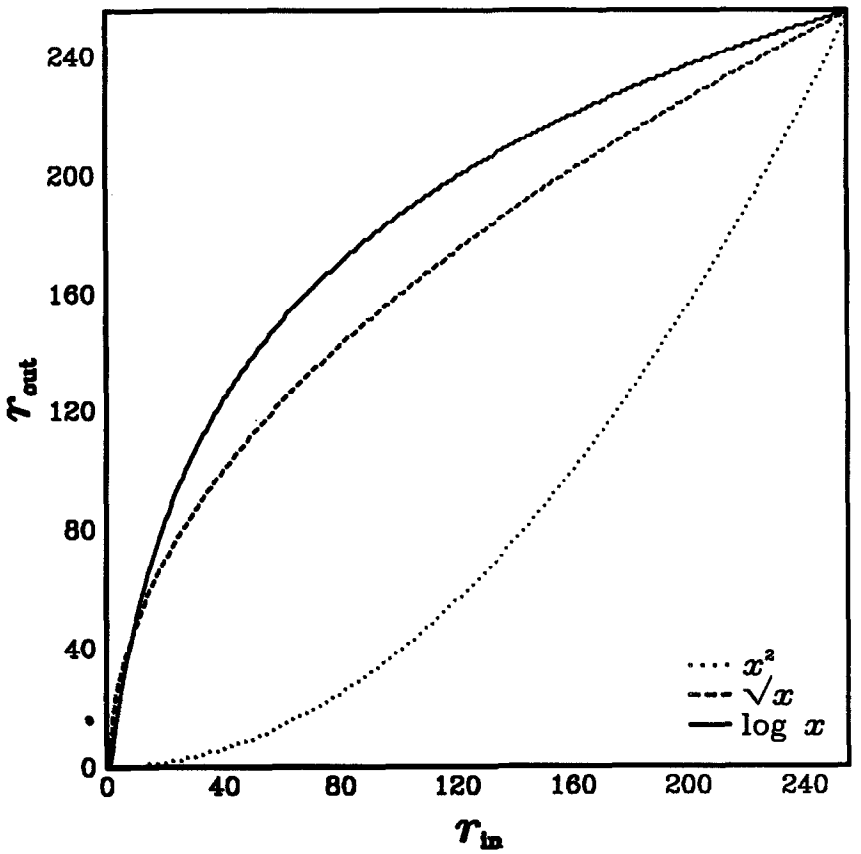


Fig. 8. Look-up tables used in the non-linear contrast enhancement of reflectance scans.

scan was generated across a crater containing floor material 20% darker than the surroundings. Figure 12 shows a profile derived from this scan by fixing $r^*$ at the value appropriate to the walls and flanks of the crater.

### 5.3.2. *Surface Photometric Function*

If surface material is dark and macroscopically smooth then reasonably accurate profiles are possible using a Lommel–Seeliger law. For other classes of terrain, however, Hapke's equation provides a more appropriate description of surface scattering properties. The implications of applying a simple Lommel–Seeliger law in such situations are demonstrated by Figure 13, which compares crater topography with profiles derived from scans across BS, DR and BR crater terrain. Multiple scattering by high albedo regolith particles leads to significant topographic distortion of the BS profile. Here a change in $r^*$ of $-0.6\%$ is sufficient to level the rim crests but leads to a depth error of $+30\%$. The neglect of unresolved macroscopic roughness distorts the DR profile in a similar yet more severe manner; in this case, a $-3\%$ adjustment of $r^*$ is required to level the profile, but a $+40\%$ depth

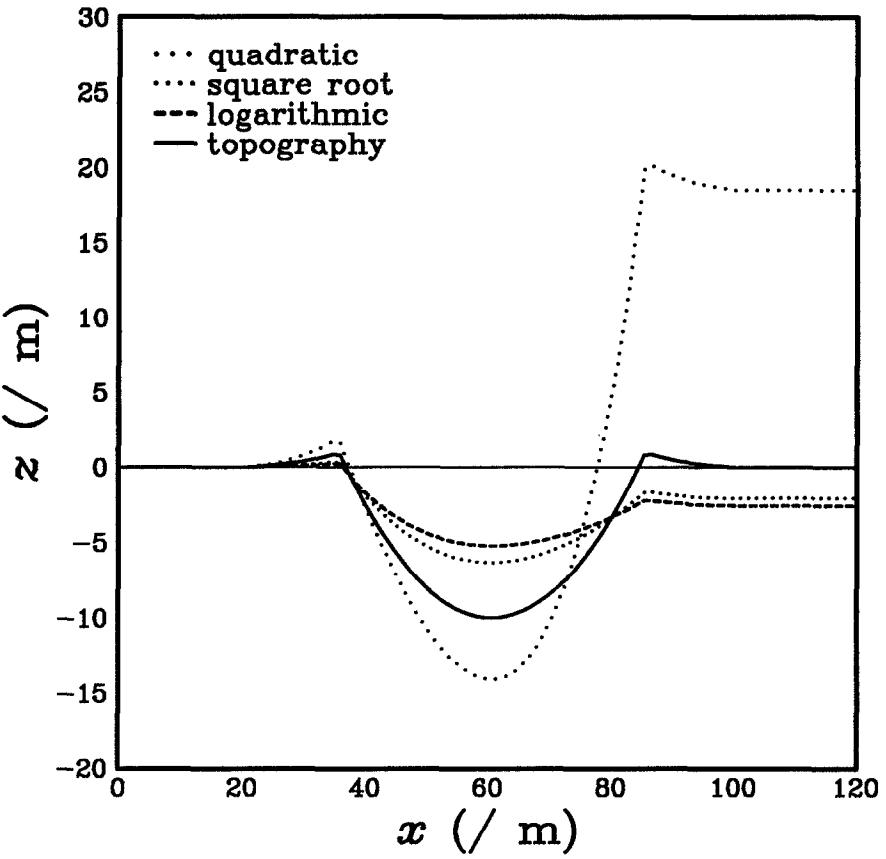


Fig. 9. The effect on crater profiles of a non-linear relationship between DN and actual surface reflectance. The results shown here were recovered from reflectance scans stretched using the look-up tables of Figure 8.

error remains and the bowl of the crater appears skewed to the left. The effects of these factors on a profile are maximised in the case of BR terrain; here, levelling results in a skewed crater whose depth is overestimated by 60%.

Given the difficulties that are associated with the application of Equation (3) to photoclinometry, it is interesting to consider whether manipulation of the empirical parameters in photometric models such as Equations (2) and (12) can produce accurate profiles. Figure 14 depicts the results of applying Minnaert's law to Hapke reflectance scans. In Figure 14a profiles across DS terrain derived using three values of $k$ are shown; good results can be achieved in the absence of significant albedo- or roughness-related effects, $k \simeq 0.6$ being appropriate here. Somewhat larger values of $k$ yield reasonable profiles across BS terrain (Figure 14b), but significant distortion of profiles across DR terrain is evident (Figure 14c) which apparently cannot be compensated for by varying $k$. Levelling of the $k = 0.6$ and $k = 0.8$ profiles in Figure 14c results in crater depth errors of $-40\%$ and $-15\%$, respectively, with a noticable asymmetry in crater shape arising in each case. In

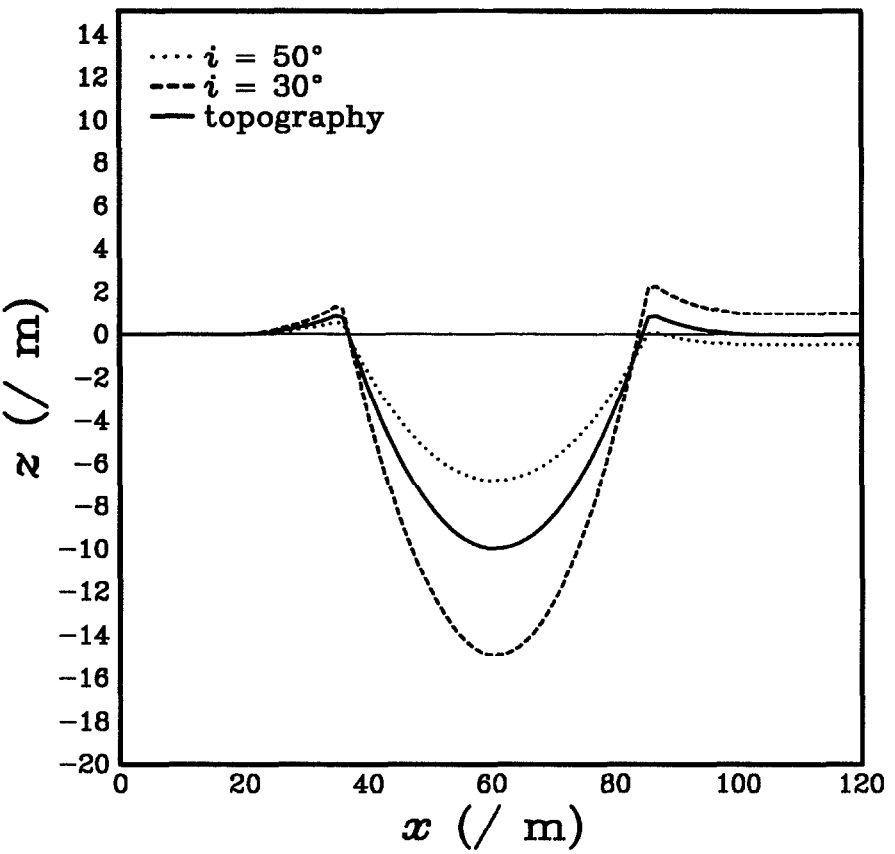


Fig. 10. The effect of errors in $i$ on recovered crater topography. The original reflectance scan was generated using a Lommel–Seeliger law at $i = 40°$; the profiles were derived using the same scattering law at $i = 30°$ and $i = 50°$.

a similar fashion, a combination of Lommel–Seeliger and Lambert scattering laws proves to be capable of producing accurate profiles across BS terrain (Figure 15a) yet incapable of dealing with dark surfaces that are rough at sub-pixel scales (such as DR terrain in Figure 15b).

### 5.3.3. *Atmospheric Scattering*

The effects of atmospheric scattering are illustrated by Figures 16 and 17. The first shows Lommel–Seeliger profiles of scans which were computed from Equation (9), nominally assuming the atmospheric parameters of Table VI. In Figure 16a one can see that crater depth is increasingly underestimated as atmospheric opacity increases. From Figure 16b it is apparent that the phase function of atmospheric scatterers can have a major effect on the results; if aerosols or suspended dust scatter almost exclusively in the forward direction ($\epsilon_a = 1.0$) then the atmosphere has little effect; however, crater depth errors increase dramatically as scattering behaviour tends toward isotropy ($\epsilon_a = 0.0$).

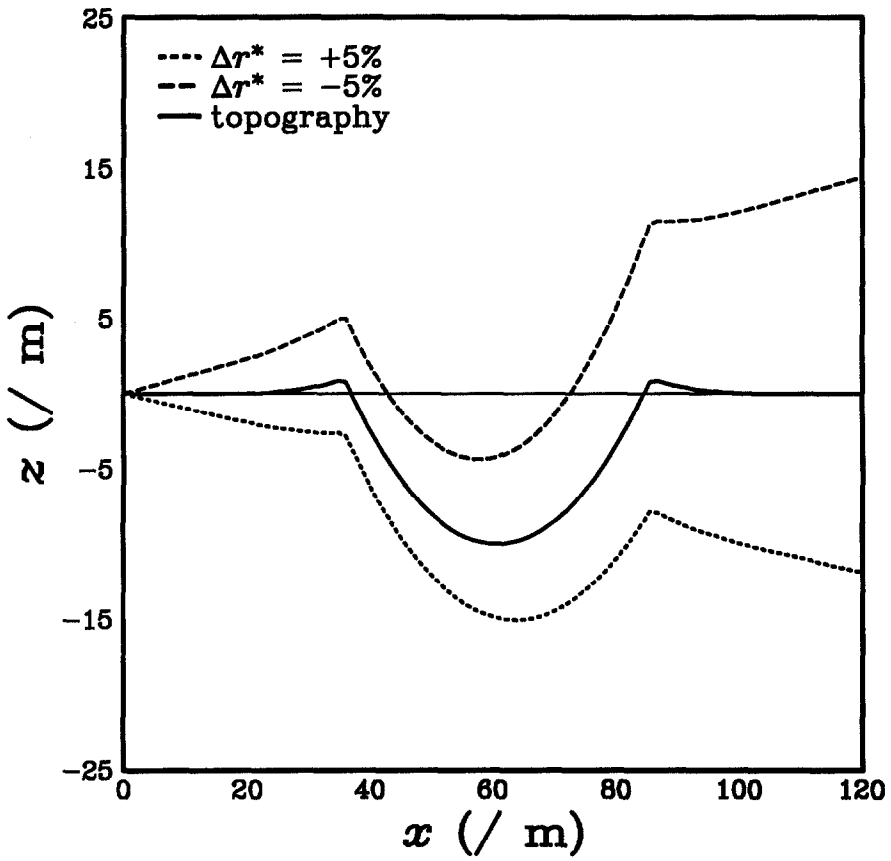


Fig. 11. The effect of errors in flat surface reflectance on topography. Errors of −5% and +5% tilt the profile roughly 6° towards and away from the illumination source, respectively.

Figure 17 shows the distortions that arise when Equations (2) and (12) are used in photoclinometry without correction for the presence of an atmosphere. The crater depth errors that remain after the levelling of the $k = 0.3$ and $k = 0.5$ profiles in Figure 17a are roughly −20% and +20%, respectively; although this suggests that an intermediate value of $k$ would allow a reasonably accurate crater depth measurement to be made, the crater itself would still appear to be strongly skewed to the left. Figure 17b demonstrates that changes to the partitioning coefficient of equation 12 cannot adequately compensate for atmospheric effects. Levelling of the $A = 1.0$ and $A = 0.5$ profiles results in crater depth errors of −30% and −50%, respectively.

### 5.4. Case Studies

Figures 18 and 19 show the results of the two case studies carried out for this paper. Figure 18 plots two Lommel–Seeliger profiles across a simulated impact

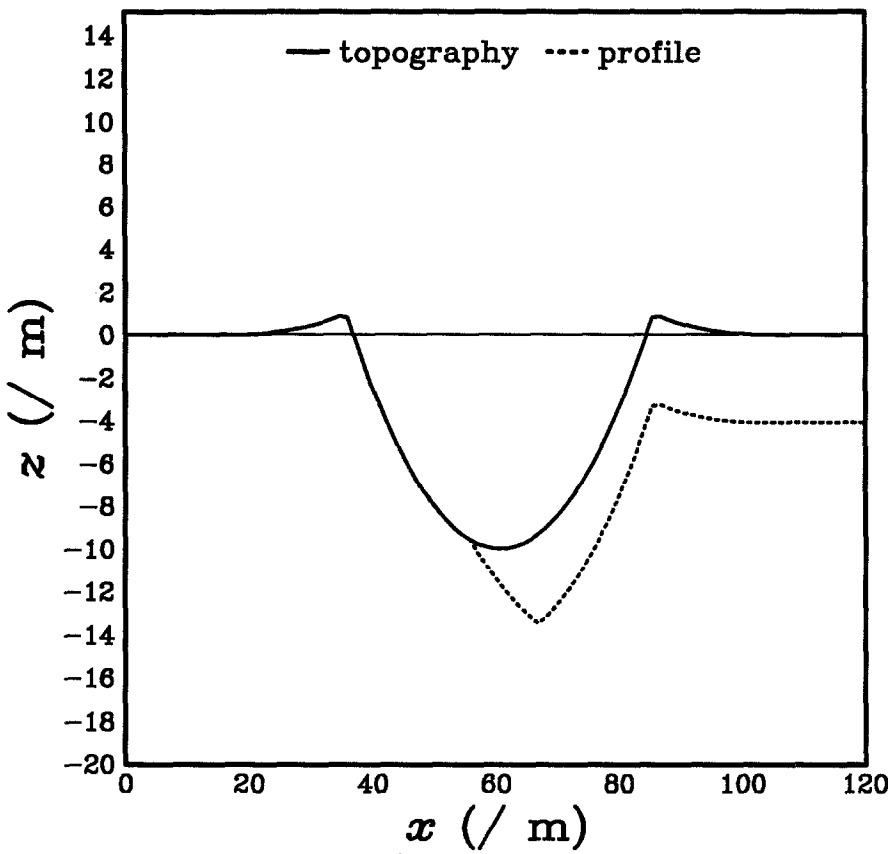


Fig. 12. Profile derived across a crater ignoring the presence of dark material on its floor.

crater on Triton; in the first, the correct flat surface reflectance was assumed; in the second, $r^*$ was adjusted so as to level the crater's rim crests. It should be noted that no real crater of comparable dimensions has been observed on Triton, simply because the highest resolution attained by VOYAGER 2 during its flyby was 0.8 km per line pair, with global coverage of the satellite achieved only at 1.5–3 km per line pair (Smith *et al.*, 1989). Nevertheless, craters smaller than about 11 km in diameter appear to possess a simple morphology and depth-diameter ratios comparable to the hypothetical structure analysed here (Strom *et al.*, 1990); similar distortions can therefore be expected in photoclinometric profiles across small craters visible in the VOYAGER images when oversimplified photometric functions are used. Figure 19 plots profiles derived using a Lommel–Seeliger law from a reflectance scan across a Bingham rheology lava flow on Mars; in the first, the correct flat surface reflectance was assumed; in the second, $r^*$ was adjusted until the levee crests had the same relative elevation, following Moore and Davis (1990).

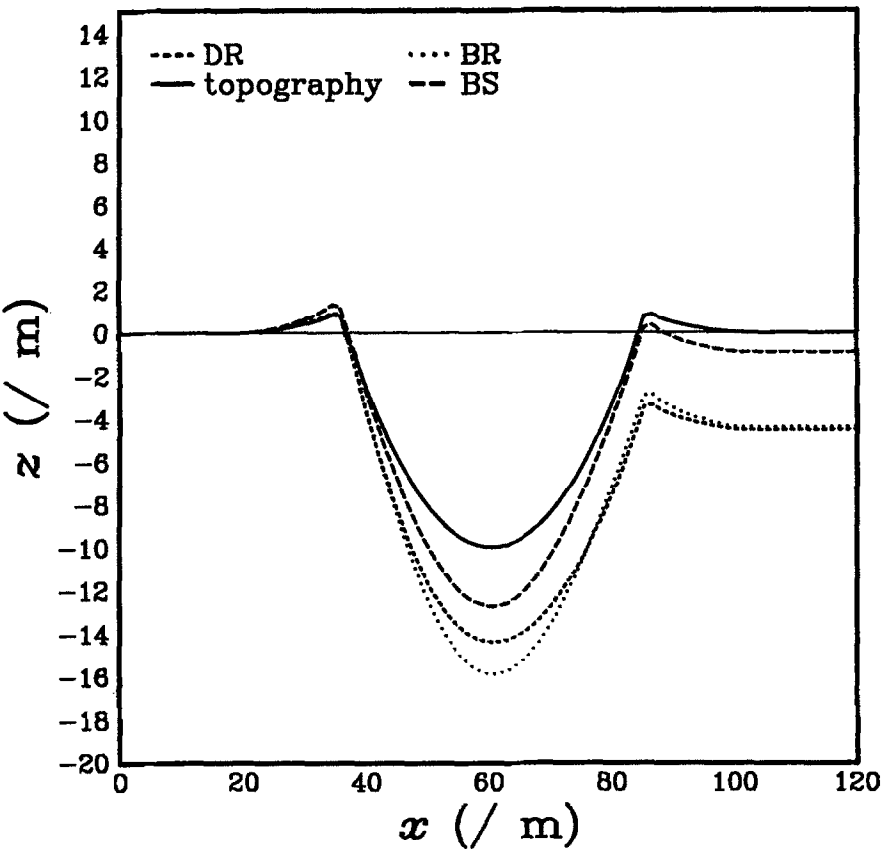


Fig. 13. Comparison of crater topography with Lommel- Seeliger profiles across BS, DR and BR terrain.

## 6. Discussion

### 6.1. Instrumental factors

Of the instrumental factors listed in Table I, digitisation and pixel noise errors have not been modelled here. One would expect the former to arise only in situations where the image as a whole is poorly exposed or where the range of reflectances characterising the region of interest has been compressed into a relatively small range of DN, possibly by the presence of high albedo terrain (e.g., the martian polar caps) in the scene. In all but the worst cases, the principal effect is likely to be a reduction in the smoothness of height variations along the profile. Pixel noise, for the reasons discussed in Section 4, is unlikely to have a major effect on derived topography. In any case, the images most affected by digitisation and noise will probably not be selected for photoclinometric analysis.

For the simulation depicted in Figure 7, unrealistically large background levels were required to produce significant errors in crater depth. One would expect a

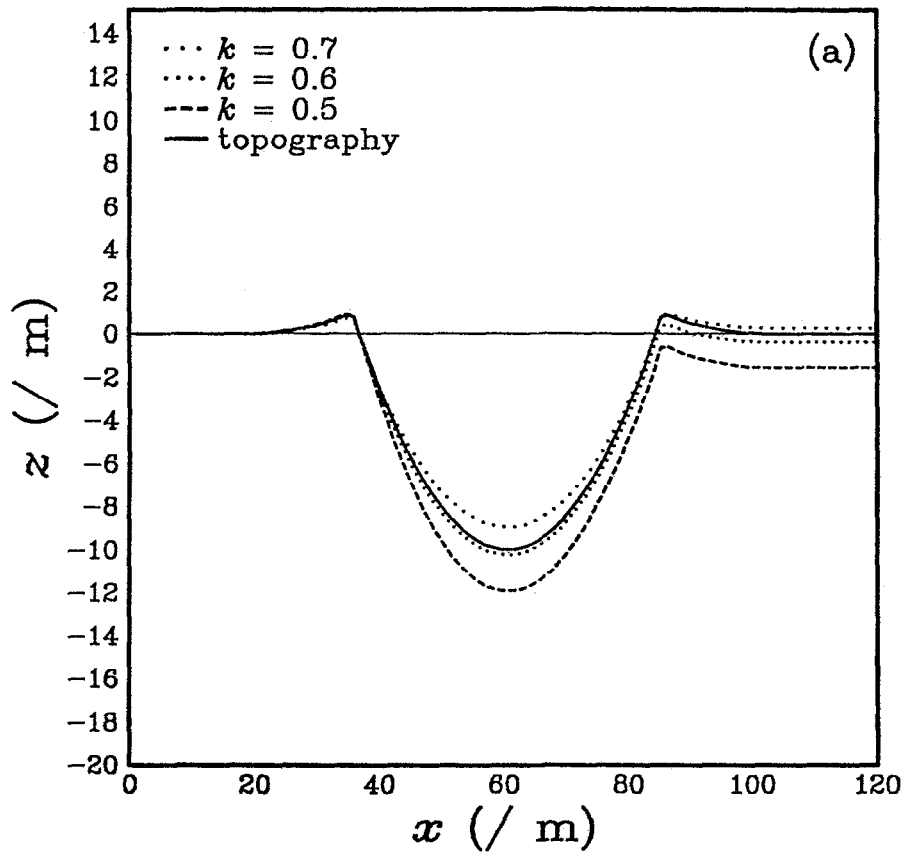


Fig. 14. Results of profiling different types of terrain using a Minnaert law with various values of $k$. Figures a and b, for DS and BS terrain, respectively, demonstrate that a Minnaert formulation can deal with smooth surfaces of low or high albedo; figure c, for DR terrain, shows the distortions that arise when roughness is introduced.

residual dark current to amount to no more than a few DN units in most cases, leading to a maximum crater depth error of a few percent. The effects of sensor response or accidental contrast stretching are potentially more serious, however; the former is almost linear in VIKING Orbiter images (Thorpe, 1976), but this is not so in the case of data acquired by the VOYAGER vidicon cameras; the latter possibility will not affect the results of photoclinometry provided that the enhancement is linear in nature and does not result in saturation at either end of the DN scale. The results presented in Figure 9 serve to underline the importance of knowing the pedigree of the original data; the images used in photoclinometry should be carefully calibrated but otherwise unprocessed.

### 6.2. Geometric factors

Scanline misalignment was not studied here, but its effects have been investigated by Jankowski and Squyres (1990). They note that errors are likely to be significant

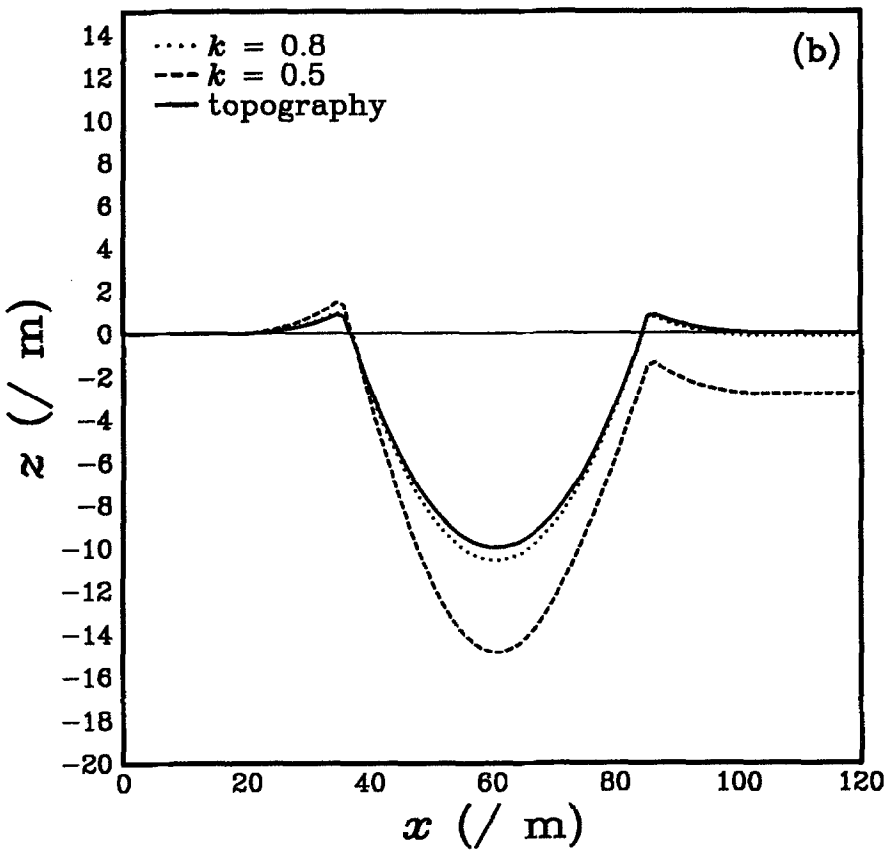


Fig. 14(b).

if the angle between the scan and the direction of dip of the slopes is greater than about 10°. They have also found that errors tend to be reduced when scans are taken parallel or nearly parallel to photometric latitude lines. One may say in general that reflectance scans should be extracted along lines parallel to the direction of illumination but perpendicular to slope strike. Satisfying these criteria will not be a problem when profiling features possessing approximate cylindrical symmetry (e.g., craters, volcanic domes or calderas), since any scan passing through the centre of the feature will lie perpendicular to the strike of the slopes; however, in the case of linear features (e.g., channels, graben or escarpments) there may be a large angle between a cross-section and a scan extracted parallel to the incident light rays.

Errors in photometric geometry are likely to be small provided that the positions of the Sun and spacecraft, camera pointing and the shape of the reference surface are known with sufficient accuracy. Discrepancies may arise, however, in situations where resolution is low, the profile is exceptionally long or the target body is small and irregular; here, variations in $i$ and $e$ along the profile must be properly

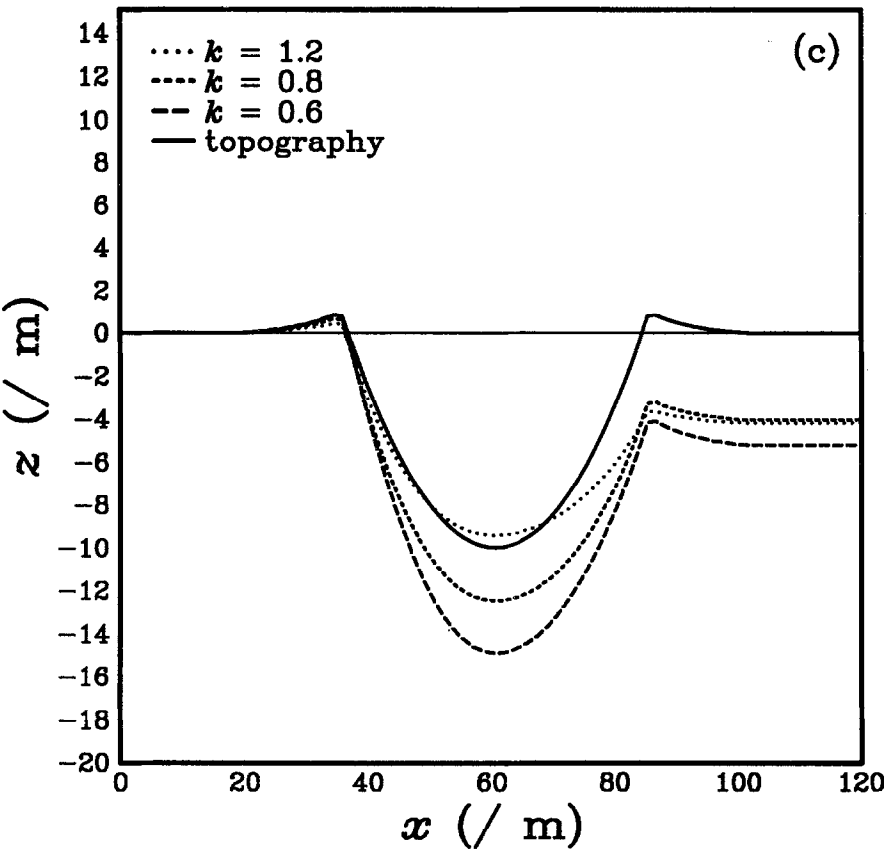


Fig. 14(c).

accounted for. In the case of an irregular body such as Phobos, this can be achieved through the use of figure models more accurate than the traditional but rather crude triaxial ellipsoid. Duxbury (1989) has published details of a spherical harmonic expansion for the radius of Phobos, with which it should prove possible to compute regional surface normals for use in the photoclinometric determination of groove and crater topography from Viking and Phobos 2 imagery.

### 6.3. Environmental Factors

#### 6.3.1. *Flat Surface Reflectance*

Figure 11 indicates that the results of photoclinometry depend sensitively on the value chosen for flat surface reflectance, making its accurate estimation important. One approach to this problem utilises Hapke's equation to compute the theoretical flat surface reflectance of terrain crossed by the scan. This necessitates the identification of all photometrically-distinct terrain classes crossed, together with the specification of appropriate Hapke parameters for each of those classes. The former can only be achieved reliably if multispectral, multiple-phase angle obser-

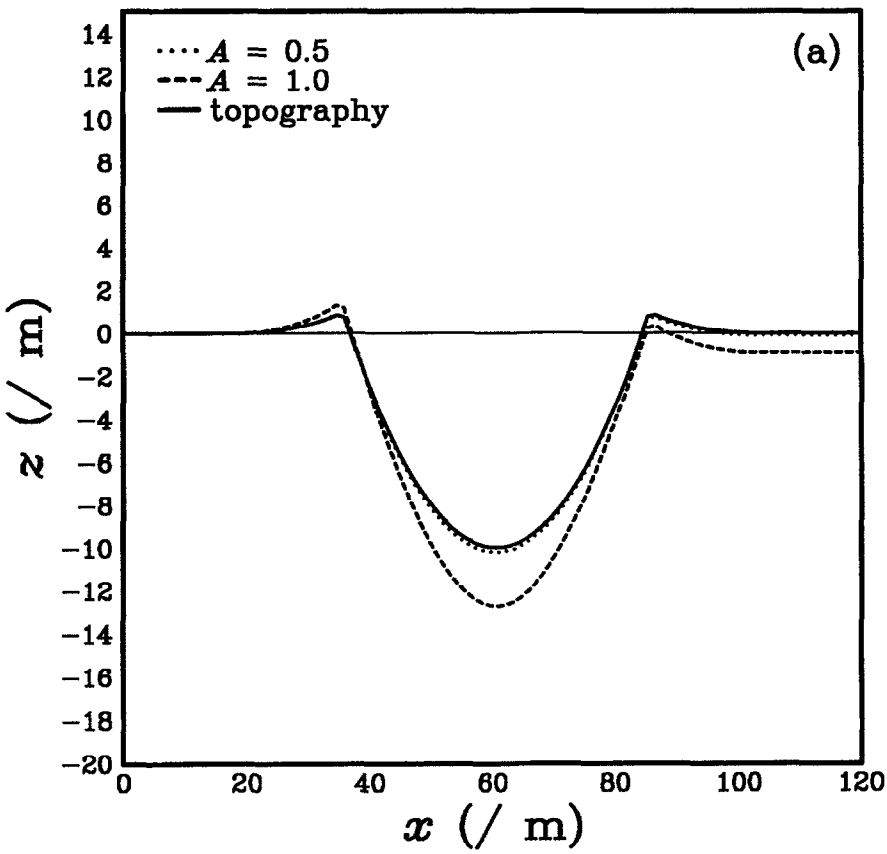


Fig. 15. Results of profiling different types of terrain using a combination of Lommel–Seeliger and Lambert laws. Figure a shows that accurate profiles are possible across smooth, high albedo terrain; figure b illustrates that this combined scattering law cannot cope with the effects of unresolved macroscopic roughness.

vations exist of the region under study; the latter requires that such observations be extensive enough to permit the fitting of Hapke's equation to reflectance datasets compiled for each type of terrain. This option is unlikely to be practical in many situations; disk-integrated photometric parameters are frequently the best that are available for planetary satellites, and their use in photoclinometry assumes firstly that extrapolation to the disk-resolved case is valid, and secondly that the region studied has homogeneous photometric properties.

Less desirable alternatives involve the use of the mean reflectance of a scan as an estimator of flat surface reflectance (Squyres, 1981; Howard *et al.*, 1982; Schenk, 1989), the manual selection of regions in the image which are taken to be flat (Jantunen and Raitala, 1983) or the specification of points along the profile having a common elevation (Mouginis-Mark and Wilson, 1981; Davis and Soderblom, 1984; McEwen, 1985). The dangers inherent in the use of mean reflectance, $\langle r \rangle$, may be demonstrated by generating scans of crater topography

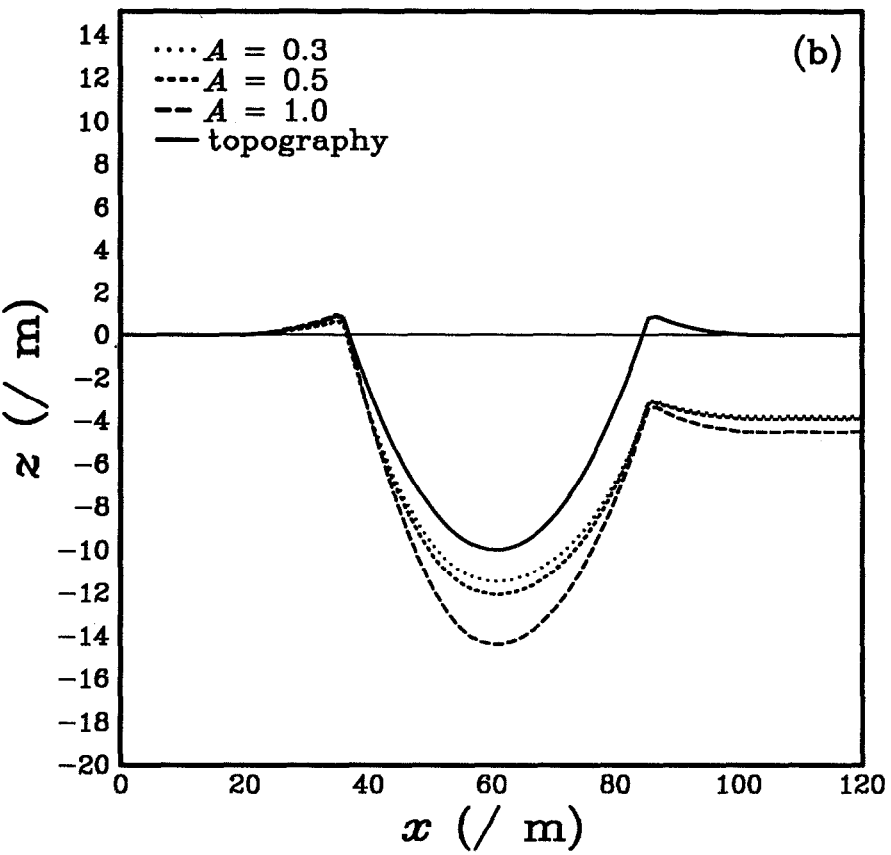


Fig. 15(b).

using Equation (4) and a range of photometric roughnesses, and then plotting $\langle r \rangle$ versus $\bar{\theta}$. Figure 20 is just such a plot. The dotted horizontal line at $\langle r \rangle = 127$ refers to a flat surface. Clearly, the discrepancy between mean reflectance and flat surface reflectance increases as the unresolved roughness of the surface increases. For values of $\bar{\theta}$ around 20°, thought to be appropriate to a variety of surfaces in the solar system (Simonelli and Veverka, 1986; Helfenstein and Veverka, 1987; Veverka *et al.*, 1987; Helfenstein *et al.*, 1988), the difference is sufficient to tilt the profiled regions of a genuinely flat surface by a few degrees.

The criterion of approximate topographic symmetry may be satisfied easily by varying $r^*$, whether or not errors in this quantity are truly responsible for the distortions apparent in photoclinometric profiles. If the distortions arise from some other source – such as the selection of an inappropriate photometric function or the neglect of an atmosphere – then fractional errors similar to those quoted in Section 5 can be expected. It is important to consider whether the erroneous adjustment of $r^*$ can be detected in any way. Figure 21, plotted with no vertical exaggeration, indicates that this is unlikely. This diagram compares crater topogra-

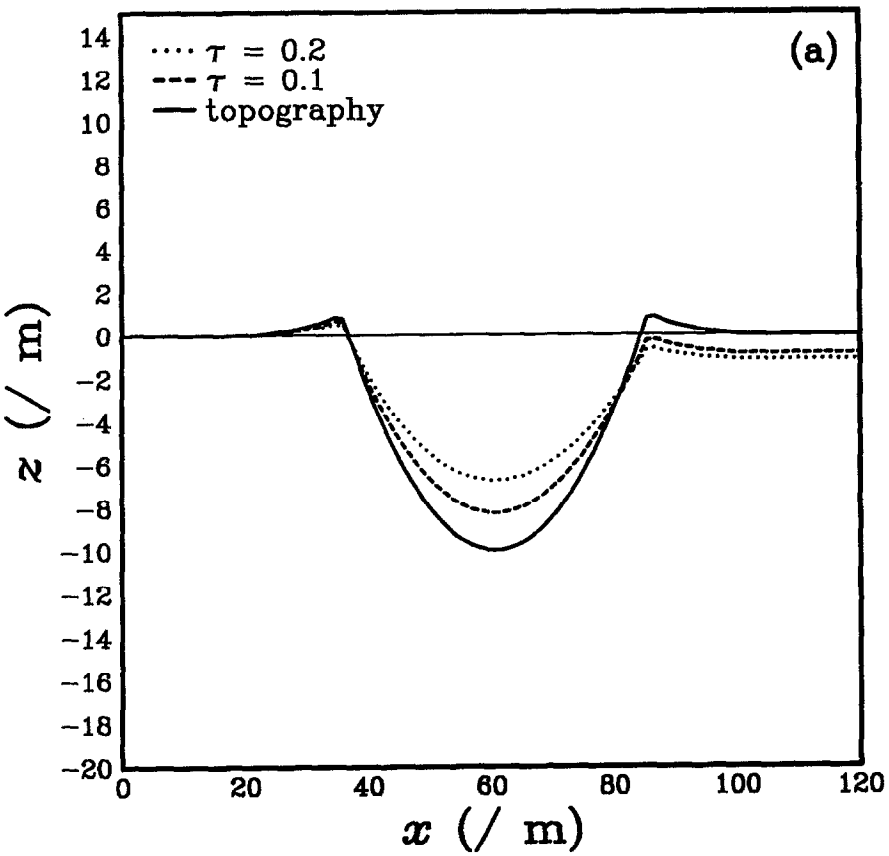


Fig. 16. Effect of atmospheric scattering on crater profiles derived assuming a Lommel–Seeliger law. Figure a plots profiles for two different optical depths; figure b plots profiles for an atmosphere exhibiting varying degrees of forward scattering.

phy with a Lommel–Seeliger profile across DR terrain, derived by adjusting $r^*$ so as to level the crater's rim crests. The levelling process has imparted a regional tilt to the profile which, although detectable here, is probably too gentle to be noticed in real situations where the feature of interest will have been emplaced on undulating background topography.

The likelihood that albedo variations along the profile will have to be dealt with is low for bodies such as Mercury, Phobos or Enceladus, but much higher in the case of Io, Ganymede or Triton. In many situations, the morphology of the features associated with observed contrasts in reflectance provides the cue needed in order to decide whether topography or albedo variations are responsible; examples of this are the high albedo ejecta blankets of some craters, the dark material found in the floors of craters on Phobos, or the low albedo aeolian surface streaks observed on Mars and Triton. Other situations are conceivable, however, in which the phenomenon responsible for reflectance contrasts is not so obvious; slumping might expose lighter or darker material on slopes, for example.

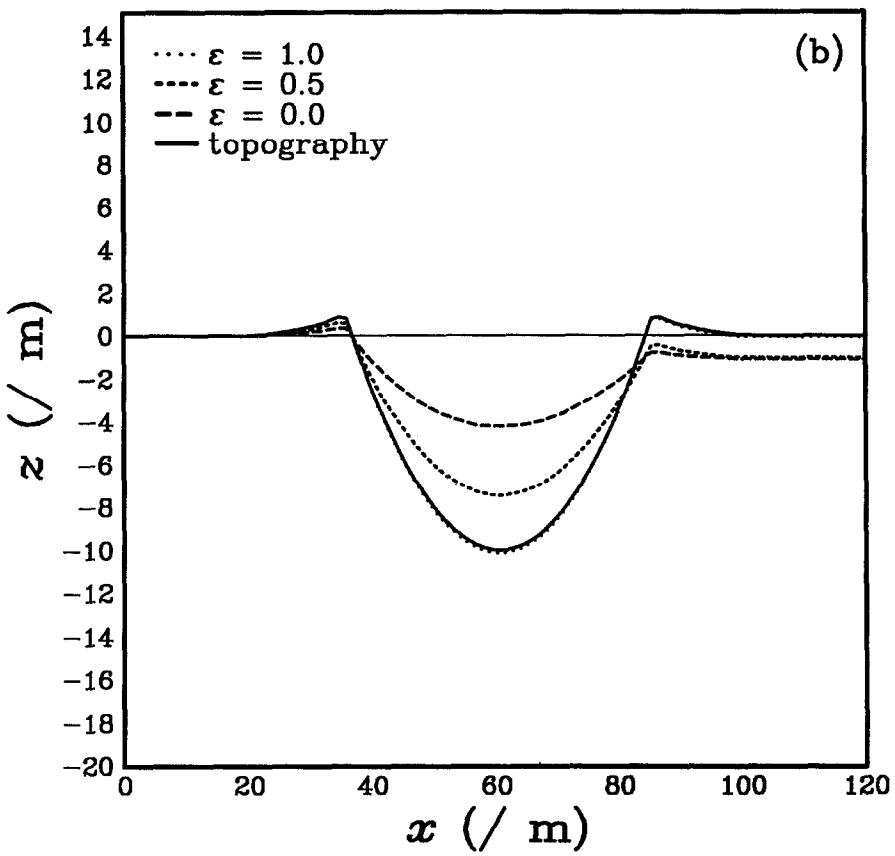


Fig. 16(b).

Topography and albedo are best distinguished by the application of classification techniques such as histogram and scattergram density slicing (e.g., Nelson *et al.*, 1986), band ratioing (e.g., Johnson *et al.*, 1983) or unsupervised clustering (Goldberg and Shlien, 1978; McEwen, 1988) to multispectral data-sets. Whether such data are available depends largely on the nature of the mission from whence they came; extensive multispectral imaging is typically carried out only during the far encounter phase of fly-bys, but it may regularly occur on orbiting spacecraft.

### 6.3.2. *Surface Photometric Function*

The errors in profiles that relate to the choice of a surface photometric function are caused largely by a failure to model either multiple scattering, unresolved roughness or both of these phenomena. The contribution of the former to observed reflectance varies as $w^n$, where $n$ is the number of times a light ray is scattered before reaching the detector, so multiple scattering is only important at high particle albedos. Furthermore, since multiply-scattered light tends to bathe particles in the regolith uniformly, scattering will become more isotropic as $w$ increases

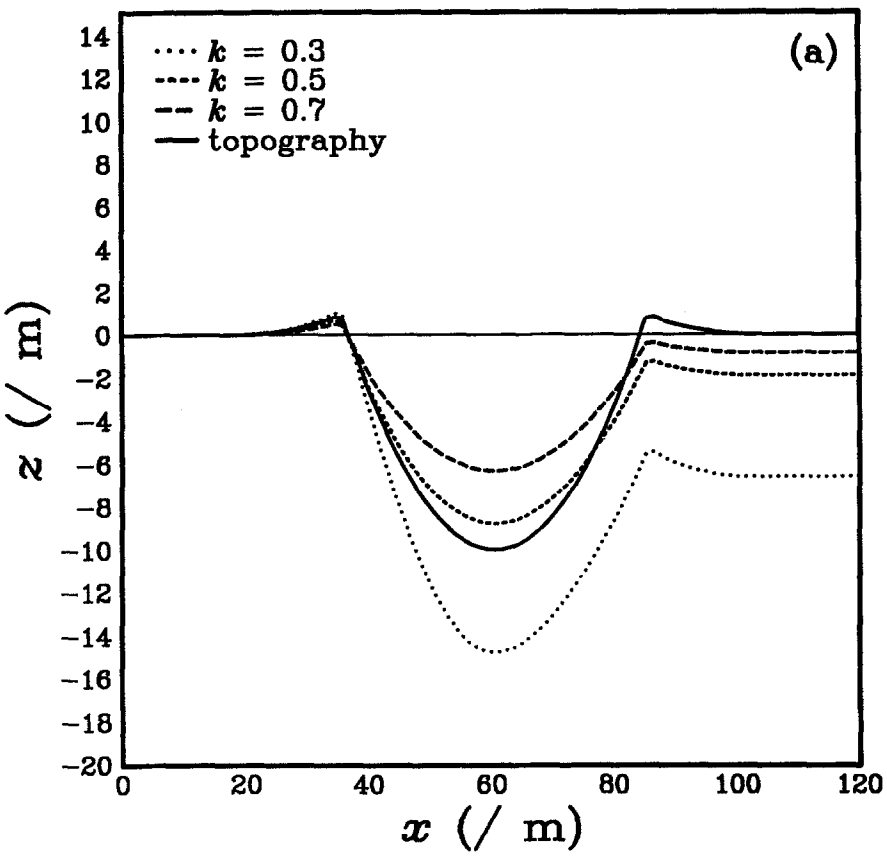


Fig. 17. Results of using Equations (2) and (12) to profile a crater in the presence of an atmosphere. Figure a shows Minnaert profiles derived for three values of $k$; figure b shows profiles derived assuming behaviour which is purely Lommel-Seeliger and half Lommel–Seeliger, half Lambert.

towards unity. This explains why Equations (2) and (12) are capable of producing accurate profiles across BS terrain; as $k$ increases towards unity or $A$ approaches zero, the behaviour modelled by these equations becomes increasingly Lambertian and, hence, more isotropic in nature.

From Figures 13–15, it is evident that unresolved roughness exerts its effect mainly on the portion of a crater profile that faces away from the source of illumination. This can be understood by noting that the larger local incidence angles on this side of the crater lead to the darkening of pixels through enhanced sub-pixel shadowing. When profiling is performed without a correction for roughness, these particular pixels are interpreted as having increased tilts away from the illumination source. Equations (3), (2) and (12) cannot adequately compensate for roughness effects; however, Equations (2) and (12) feature empirical parameters which can be varied in conjunction with $r^*$ to reduce the errors in elevation for a single feature. Such a reduction may be at the expense of both the symmetry

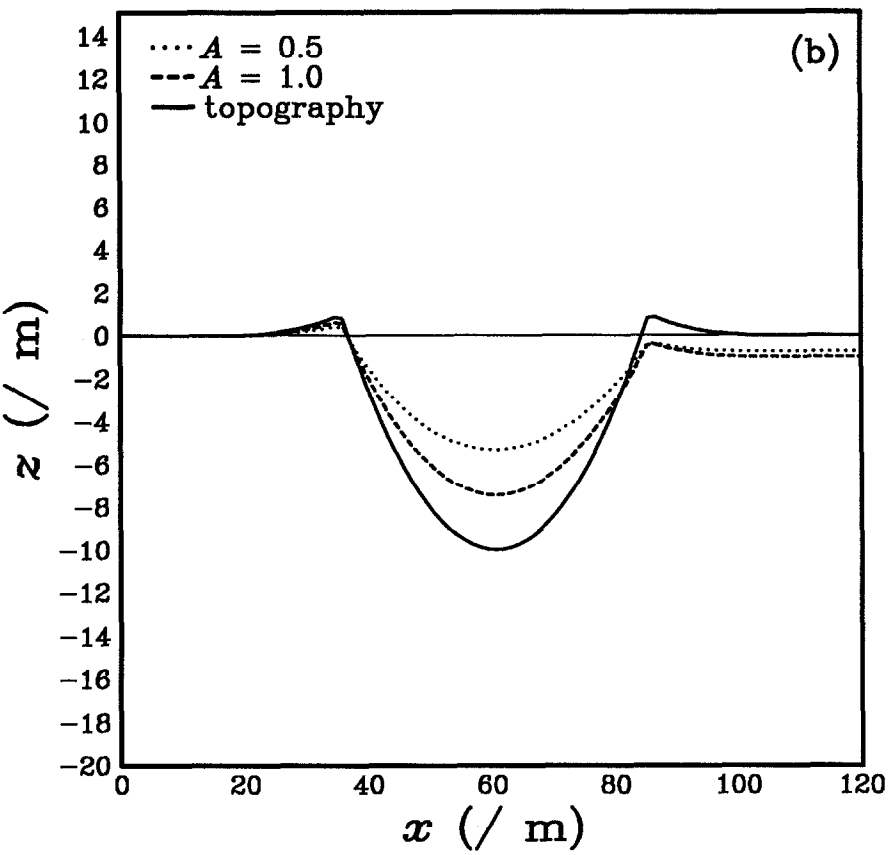


Fig. 17(b).

of the profile and the accuracy with which other landforms are rendered in long profiles that cross several features of interest.

Insights into the extent to which the choice of a photometric function may have affected other workers' results come from considering the types of surface material conceivably modelled by the four generic terrain classes studied here. An obvious correlation exists between observed geometric or normal albedo and the average single-scattering albedo of planetary regoliths. In this respect, the surfaces of dark bodies – Phobos and Deimos, C class asteroids, Amalthea – resemble DS or DR terrain, whereas the most reflective objects – Europa, Enceladus, Triton – merit a BS or BR description. The near-ubiquity of impact cratering as a geomorphic agent on the solid-surfaced planets and satellites suggests that comparatively young, resurfaced terrain is better described by the DS or BS classes, whilst DR or BR would more appropriately classify ancient, heavily cratered units.

The results of photometric investigations are in broad agreement with the interpretation above. Single-scattering albedos close to 0.1 have been estimated for Phobos (Efford, 1989, 1990) and for the lunar maria (Helfenstein and Veverka,

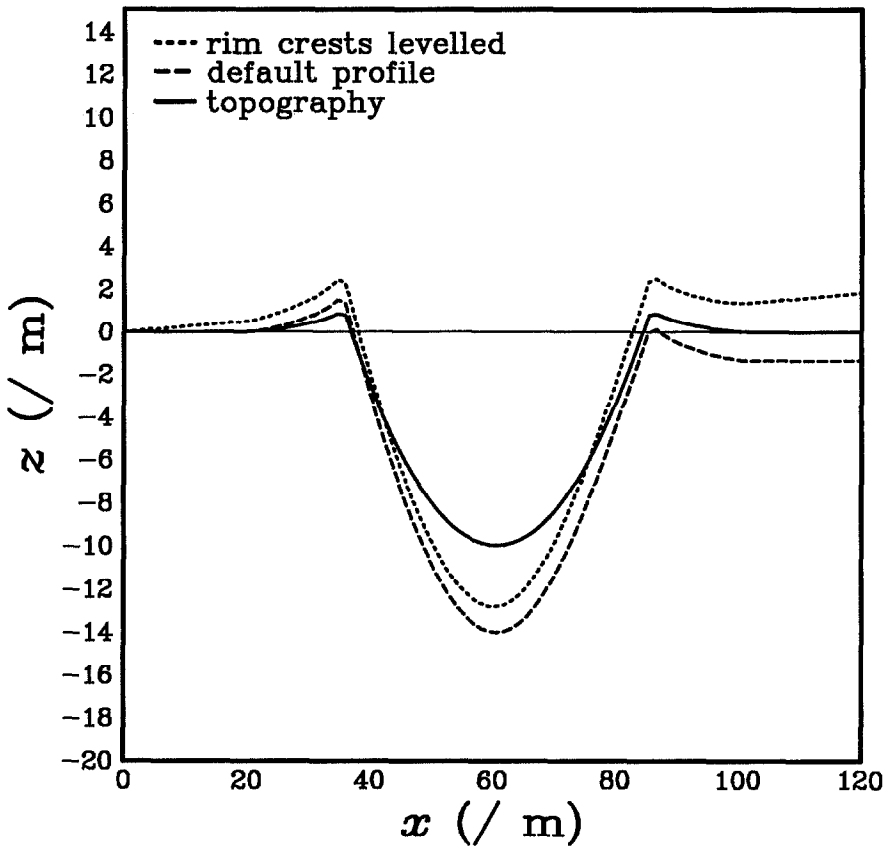


Fig. 18. Profiles across a hypothetical impact crater on Triton, derived assuming a Lommel–Seeliger law.

1987), whereas studies of Europa and Enceladus suggest particle albedos of 0.97 and 0.99, respectively (Buratti, 1985). Resurfaced regions of the Moon and Ganymede appear to be characterised on average by $\bar{\theta}$ values of 8° and 3°, respectively – considerably less than roughness estimates for the visibly older terrain also present on the surfaces of these satellites (Helfenstein, 1986; Helfenstein and Veverka, 1987).

Resurfaced terrain is not photometrically smooth, probably because it is subsequently peppered by small craters and, on the smallest scales, gardened by micrometeoroid impacts. The surface texture of flows from effusive volcanic eruptions could further contribute to optical measures of roughness (Efford, 1990), which may partially explain the anomalously high values of $\bar{\theta}$ estimated for Io (Simonelli and Veverka, 1986). The non-negligible $\bar{\theta}$ of young planetary terrains suggests that roughness effects may become noticable if incidence angles are large enough. This raises an important point: moderately large $i$ is desirable in order to optimise the sensitivity of photoclinometry to subtle changes in tilt (Jankowski and Squyres,

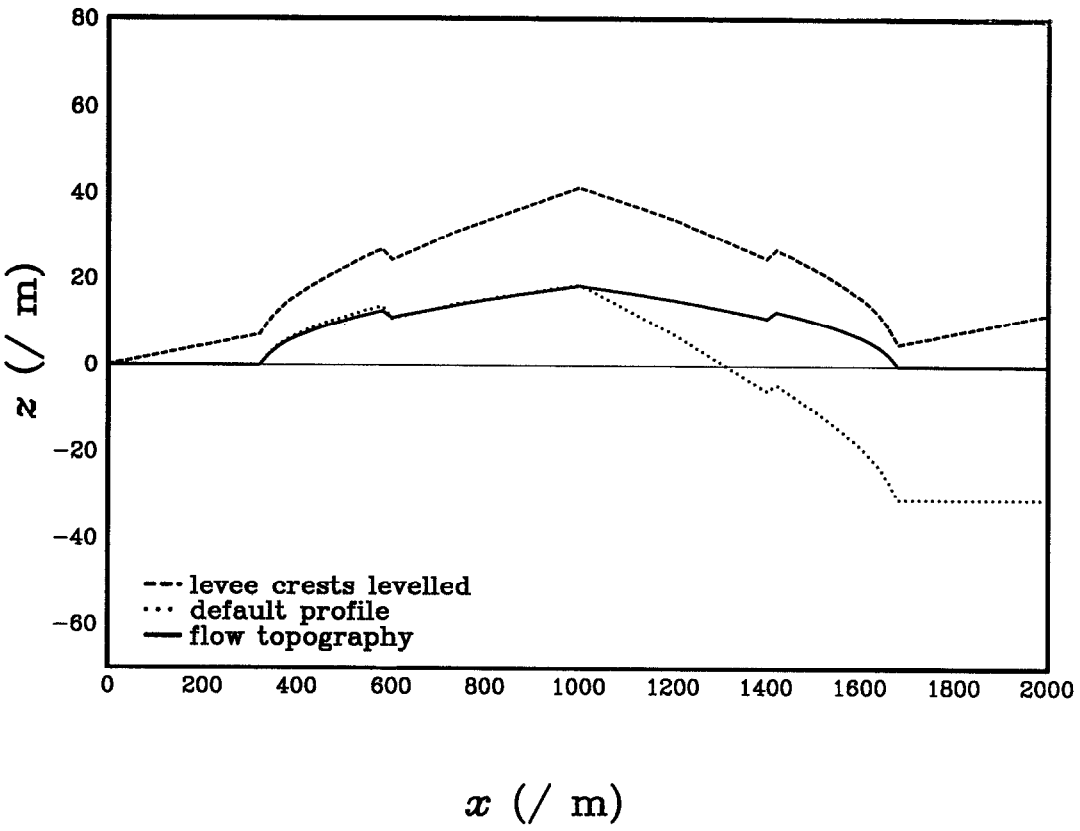


Fig. 19. Profiles across a synthetic Bingham lava flow on Mars, derived assuming a Lommel-Seeliger law.

1990), but such conditions increase the likelihood that roughness effects will be significant.

Some general comments can now be made regarding profiles derived across features on atmosphereless bodies. Those utilising a pure Lommel-Seeliger law can be accurate only in cases where apparently smooth, low albedo terrain – the lunar maria, for example – is under study. As discussed earlier, a Minnaert law or a combination of Lommel-Seeliger and Lambert laws can deal adequately with multiple scattering effects; thus the choice of these photometric models should exert a minimal influence on profiles across young low or high albedo terrain, provided that $i$ is modest in size. Isolated exceptions to this rule could include regions of Io and bright, fresh craters on Ganymede – which are probably roughened photometrically by ejecta (Helfenstein, 1986). No simple photometric function can be trusted to give satisfactory results when applied to more ancient terrain, to units with an uncertain origin and geologic history, or to the majority of natural planetary surfaces when illuminated at large incidence angles.

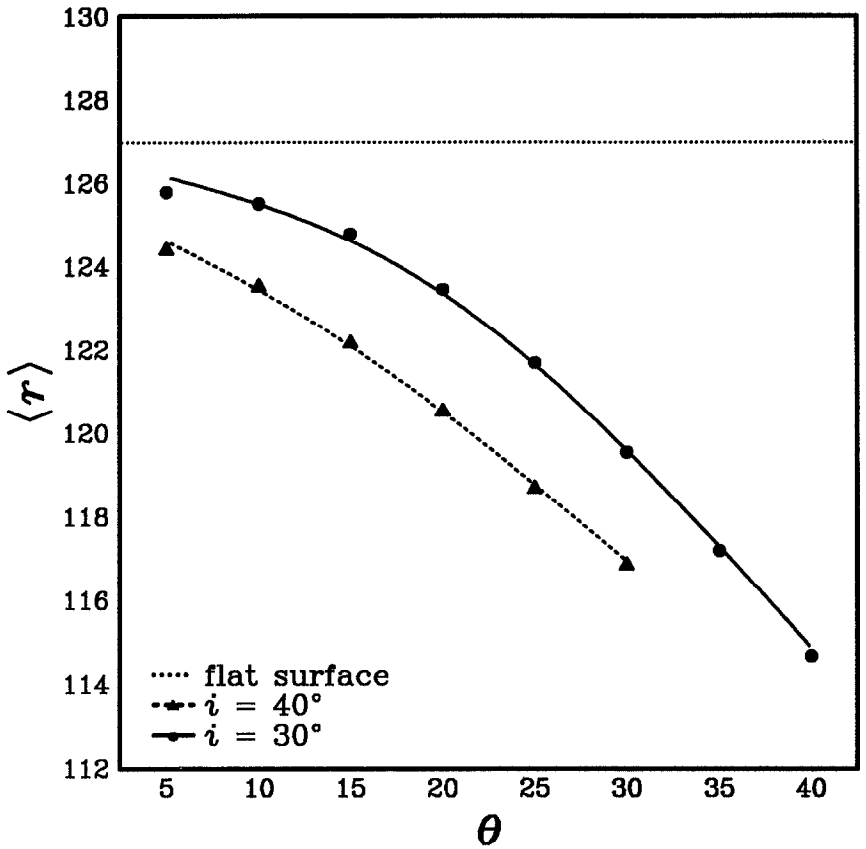


Fig. 20. Effect of unresolved roughness on the mean reflectance of a scan. As $\bar{\theta}$ increases, so too does the discrepancy between $\langle r \rangle$ and the true flat surface reflectance, $r^*$.

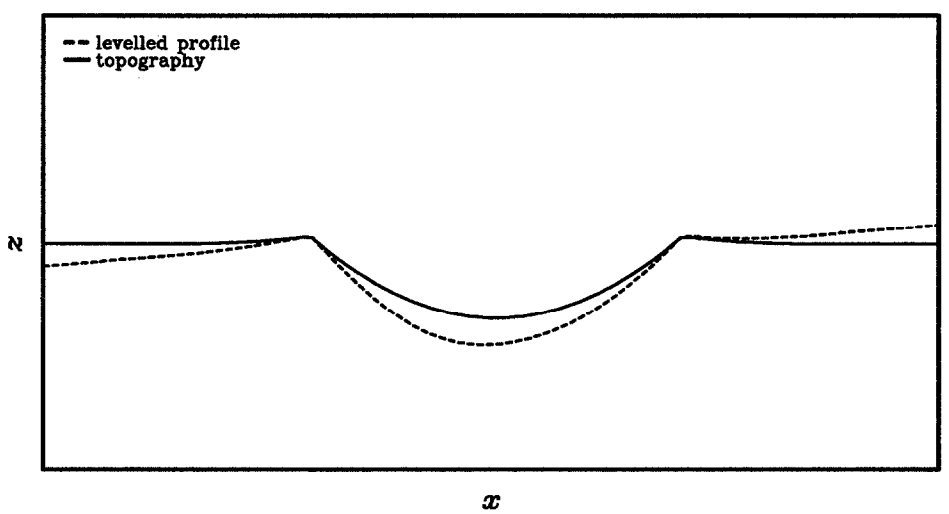


Fig. 21. Comparison of crater topography and a levelled Lommel–Seeliger profile of DR terrain.

### 6.3.3. *Atmospheric Scattering*

An approach more rigorous than that adopted here (e.g., Lee and Clancy, 1990; Hillier *et al.*, 1990) would account for higher-order scattering by the atmosphere and coupling between it and the surface. Nevertheless, the results of this study are in accordance with expectations; errors in photoclinometry become more significant as optical depth increases; errors are reduced as scattering by aerosols or suspended dust becomes increasingly forward-biased, largely because more forward scattering atmospheres are more transparent to incoming and outgoing radiation. Studies by Lee and Clancy (1990) have emphasised an important point: a constant atmospheric correction is inapplicable, even within a single region of an image or for a single value of $\tau$. The errors that accrue when constant corrections are applied are therefore likely to be greater than has been previously anticipated, by Tanaka and Davis (1988) or Jankowski and Squyres (1990), for example. A further complication comes from the temporal variability of atmospheric scattering; here $w_a$ and $\epsilon_a$ are likely to remain relatively constant over time, making $\tau$ the principal unknown.

In the case of Mars, where the Viking Orbiters have provided a large dataset, the following strategy will help to avoid the problems associated with atmospheric scattering. The starting point should be a set of images of the same scene viewed and illuminated similarly, but acquired at different times. Following Kahn *et al.* (1986), the locations of features near the limit of resolution should be mapped in each image; the image for which the largest number of features can be identified will have the lowest atmospheric opacity, and should hence be used in further analyses. Measuring the intensity of light scattered into the true shadows found in this image (cf., Tanaka and Davis, 1988) should allow reasonable estimates of $\tau$ to be made, provided that realistic values of $w_a$ and $\epsilon_a$ are assumed. Profiling of scans extracted from the image may then be carried out, using Equation (9).

## 6.4. Case studies

The motivation for specific case studies comes mainly from the need to assess, firstly, the magnitude of possible errors in past and future work involving photoclinometry and, secondly, the implications that these errors might have for the conclusions drawn from such work. On bodies possessing atmospheres, scattering by the surface and by the atmosphere cannot be considered in isolation. Figures 13 and 16 collectively suggest that the errors induced by the use of an oversimplified photometric function and by the neglect of atmospheric scattering may partially or wholly cancel one another out; whether this occurs or not will depend on the particular set of photometric parameters characterising the surface and the atmosphere. In the case of a crater on Triton the net effect of neglecting surface roughness, a high particle albedo and atmospheric haze is a 45% overestimate of crater depth, as Figure 18 illustrates.

The second case study was carried out with a more specific aim in mind: an

TABLE VII

Errors in photoclinometric measurements of martian lava flow morphology, and the resulting errors in the inferred rheological properties of the flow

| Quantity | | Error (%) |
|---|---|---|
| Morphology | $W$ | 1.5 |
| | $W_c$ | 2.4 |
| | $d_c$ | 84 |
| | $d_b$ | 53 |
| Rheology | $S_y$ | 119 |
| | $F$ | 53 |
| | $\eta$ | 157 |

assessment of how errors in photoclinometric flow thickness measurements affect the inferred rheological properties of martian lavas. Errors in the centreline depth, $d_c$, and levee depth, $d_b$, of the flow were found by comparing values for these parameters measured from the levelled Lommel–Seeliger profile in Figure 19 with the original flow topography. Table VII lists the fractional errors in $d_c$ and $d_b$, along with the fractional errors in width measurements that result from the digitised nature of the scan and profile. The influence of these errors on yield strength estimates can be determined by noting that

$$S_y = \frac{\rho g d_c^2}{W}. \tag{13}$$

This expression was first applied to ice sheets by Orowan (1949), but it is viable for any Bingham plastic. Hulme (1974) derived analogous equations for $S_y$ that involve the slope of the terrain resolved along the flow; Equation (13) is preferable, however, primarily because the sparse stereoscopic coverage for many areas of Mars where flows are observed poorly constrains regional slope estimates (Fagents and Wilson, 1990). Ironically, the simple photoclinometric methods discussed here cannot provide better estimates, because the most favourable conditions for flow thickness measurement (illumination direction parallel to a cross-section through the flow) are the *least* favourable for the determination of the slopes down which the flow front advanced.

If we assume that lava density and local gravitational acceleration are known, the strength errors may be expressed in terms of the errors in $d_c$ and $W$ using

$$\sigma_{S_y}^2 = \sigma_{d_c}^2 \left(\frac{\partial S_y}{\partial d_c}\right)^2 + \sigma_W^2 \left(\frac{\partial S_y}{\partial W}\right)^2. \tag{14}$$

Combination of Equation (13) and its partial derivatives with Equation (14) then gives

$$\frac{\sigma_{S_y}}{S_y} = \left[2\left(\frac{\sigma_{d_c}}{d_c}\right)^2 + \left(\frac{\sigma_W}{W}\right)^2\right]^{1/2}. \tag{15}$$

Table VII gives the fractional error in yield strength computed using the above equation.

In a similar manner, errors may be derived for the effusion rate, $F$, and apparent viscosity, $\eta$, of the flow. Expressions for these quantities, as given by Wilson and Head (1983), are

$$F = \frac{G\kappa W_c L}{d_b}, \tag{16}$$

$$\eta = \frac{1}{24F}\left(\frac{W_c^{11} S_y^5 \sin^6 \alpha}{\rho g}\right)^{1/4}, \tag{17}$$

where $\kappa$ is the thermal diffusivity of the lava, $L$ is the length of the flow, $\alpha$ is the slope down which the flow has advanced and $G$ is the *critical Graetz number*, a dimensionless parameter in problems dealing with the laminar flow of a hot fluid through a cool pipe which is thought to reach a value of 300 once flow has ceased in terrestrial lava channels (Wilson and Head, 1983). In calculating fractional errors in $F$ and $\eta$ from these equations, $G$ and $\kappa$ were assumed to be known, the flow was assumed to be long (making the fractional error in $L$ negligible) and possible errors in $\alpha$ were ignored. Table VII gives the results of error computation: clearly, the naive application of photoclinometry to Martian lava flows can lead to significant errors in their inferred rheological properties.

## 7. Conclusions

The conclusions of this study are best expressed in the form of recommendations to interpreters of previous work employing the technique and, in particular, those wishing to apply it in the future.

Digital images represent the basic data source in photoclinometry. They should undergo radiometric calibration and noise or dropout removal, but should otherwise be unprocessed. The use of images where the target body exhibits a high degree of within-frame curvature should be avoided, if at all possible. Ideally, emergence angles should be close to zero within the regions of interest in any image – a requirement more likely to be satisfied for orbiter missions than for flybys.

Scans should be extracted parallel to the direction of illumination and, if possible, perpendicular to slope strike. If the latter cannot be achieved, the slopes derived by photoclinometry will be underestimates. Scans should be short enough that regional incidence and emergence angles do not vary appreciably. If this proves to be impractical then the gradual changes in $i$ and $e$ along a scan will have to be modelled. In a simple scheme, bilinear interpolation from the latitudes and

longitudes of the image corners (commonly given in the supplementary navigational data records supplied with images) will allow the estimation of the latitude and longitude of each pixel in the scan. From these coordinates and those of the sub-spacecraft and sub-solar points, $i$ and $e$ can be calculated. For very irregular bodies such as Phobos, knowledge of the satellite's pole and orientation coupled with information on camera pointing will allow the planetocentric coordinates of any given pixel to be estimated. The normal vector to the reference surface at this location can then be derived from models for that surface such as a triaxial ellipsoid or spherical harmonic expansion. The desire to minimise integral height errors should provide further motivation for restricting the length of scans extracted from images.

Prior to profiling, an attempt should be made to identify the photometrically-distinct terrain units crossed by a scan. This is best achieved using multispectral images of the scene under study together with the results of disk-resolved photometric analyses of multiple-phase angle data. Each class of terrain identified should be assigned a unique flat surface reflectance and, if appropriate, set of photometric parameters.

In the presence of an atmosphere, Equations (9–11) should suffice to describe observed reflectances. However, caution should be exercised in the selection of a model for surface reflectance; a Lommel–Seeliger law will be inappropriate in the majority of situations; a Minnaert law should only be applied to apparently smooth, recently resurfaced terrain illuminated at modest incidence angles, and here only when knowledge of that terrain's photometric properties is too poor to warrant the use of a Hapke model.

The application of Hapke's equation in photoclinometry is hampered mainly by the fact that reasonable estimates of its parameters are available only for a select range of different planetary surfaces. Accurate estimation of the Hapke parameters is not always crucial, however; results should be relatively insensitive to the values chosen for the opposition effect parameters, $h$ and $B_0$, when $i \geqslant 40°$. In the case of photometrically-homogeneous regions of low albedo material – on Phobos, for example – simplification of equation 4 can be carried out by collecting together all the phase angle-dependent terms and neglecting the term in $H^2$. Hence

$$r(\mu_0', \mu', g) = A \frac{\mu_0'}{\mu_0' + \mu'} S(\mu_0', \mu', g) , \tag{18}$$

where $A$, constant in a single image, can be thought of as the effective albedo of the pixel under consideration. Equation (1) can then be written as

$$R = \frac{r}{r^*} = \frac{\mu_0'(\mu_0^* + \mu^*)S}{\mu_0^*(\mu_0' + \mu')S^*} , \tag{19}$$

where the prime and the asterisk denote roughness-dependent quantities calculated for tilted and locally-flat surfaces, respectively.

It is to be hoped that, in cases where the approach outlined above cannot be followed in its entirety, the comparison of photoclinometric profiles derived from real data with those presented in this paper may permit the diagnosis of the errors that may be affecting them.

## Acknowledgements

Discussions with Lionel Wilson helped to improve the style and the content of this paper. Financial support for the work herein was provided by SERC grant GR/F 76435.

## References

Arvidson, R. E., Guinness, E. A., Dale-Bannister, M. A., Adams, J., Smith, M., Christensen, P. R., and Singer, R. B.: 1989, *J. Geophys. Res.* **94**, 1573.
Buratti, B. J.: 1984, *Icarus* **59**, 392.
Buratti, B. J.: 1985, *Icarus* **61**, 208.
Davies, A. G. and Wilson, L.: 1987, *Lunar Planet. Sci. XVIII Abstract*, 221.
Davis, P. A. and McEwen, A. S.: 1984, *Lunar Planet. Sci. XV Abstract*, 194.
Davis, P. A. and Soderblom, L. A.: 1984, *J. Geophys. Res.* **89**, 9449.
Duxbury, T. C.: 1989, *Icarus* **78**, 169.
Efford, N. D.: 1989, *Lunar Planet. Sci. XX Abstract*, 262.
Efford, N. D.: 1990, Ph.D. thesis, Lancaster University, UK.
Fagents, S. A. and Wilson, L.: 1990, *Lunar Planet. Sci. XXI Abstract*, 341.
Goldberg, M. and Shlien, S.: 1978, *IEEE Trans. Sys. Man. Cyber.* **SMC-8**, 86.
Guinness, E. A., Arvidson, R. E., and Irons, J. R.: 1990, *Lunar Planet. Sci. XXI Abstract*, 441.
Hapke, B.: 1981, *J. Geophys. Res.* **86**, 3039.
Hapke, B.: 1984, *Icarus* **59**, 41.
Hapke, B.: 1986, *Icarus* **66**, 270.
Helfenstein, P.: 1986, Ph.D. thesis, Brown University, Providence RI, USA.
Helfenstein, P., and Veverka, J.: 1987, *Icarus* **72**, 342.
Helfenstein, P., Veverka, J., and Thomas, P. C.: 1988, *Icarus* **74**, 231.
Hillier, J., Helfenstein, P., Verbiscer, A., Veverka, J., Brown, R. H., Goguen, J., and Johnson, T.V.: 1990, *Science* **250**, 419.
Howard, A. D., Blasius, K. D., and Cutts, J. A.: 1982, *Icarus* **50**, 245.
Hulme, G.: 1974, *Geophys. J. RAS* **39**, 361.
Jankowski, D. and Squyres, S.: 1988, *Science* **241**, 1322.
Jankowski, D. G. and Squyres, S. W.: 1990, *Lunar Planet. Sci. XXI Abstract*, 561.
Jantunen, H. and Raitala, J.: 1983, *The Moon and the Planets* **29**, 7.
Johnson, T. V., Soderblom, L. A., Mosher, J. A., Danielson, G. E., Cook, A. F., and Kuperman, P.: 1983, *J. Geophys. Res.* **88**, 5789.
Kahn, R., Guinness, E., and Arvidson, R.: 1986, *Icarus* **66**, 22.
Lee, S. W. and Clancy, R. T.: 1990, *Lunar Planet. Sci. XXI Abstract*, 688.
Lumme, K., Martin, L. J., and Baum, W. A.: 1981, *Icarus* **45**, 379.
McEwen, A. S.: 1985, *Lunar Planet. Sci. XVI Abstract*, 528.
McEwen, A. S.: 1988, *Icarus* **73**, 385.
Minnaert, M.: 1941, *Astrophys. J.* **93**, 403.
Minnaert, M.: 1961, in G. P. Kuiper and B. M. Middlehurst (eds.), *The Solar System III. Planets and Satellites*, Univ. of Chicago Press, 213.
Moore, H. J. and Davis, P. A.: 1990, *Lunar Planet. Sci. XXI Abstract*, 805.
Moore, J., McEwen, A., Albin, E., and Greeley, R.: 1986, *Icarus* **67**, 181.
Mouginis-Mark, P. J. and Wilson, L.: 1981, *Comp. Geosci.* **7**, 35.

Nelson, M. L., McCord, T. B., Clark, R. N., Johnson, T. V., Matson, D. L., Mosher, J. A. and Soderblom, L. A.: 1986, *Icarus* **65**, 129.
Noland, M. and Veverka, J.: 1977, *Icarus* **30**, 212.
Orowan, E.: 1949, *J. Glaciol.* **1**, 231.
Passey, Q.: 1983, *Icarus* **53**, 105.
Pike, R. J. and Davis, P. A.: 1984, *Lunar Planet. Sci. XV Abstract*, 645.
Schenk, P.: 1989, *J. Geophys. Res.* **94**, 3813.
Simonelli, D. P. and Veverka, J.: 1986, *Icarus* **68**, 503.
Smith, B. A. and the Voyager imaging team: 1989, *Science* **246**, 1422.
Squyres, S.W.: 1981, *Icarus* **46**, 156.
Strom, R. G., Croft, S. K., and Boyce, J. M.: 1990, *Lunar Planet. Sci. XXI Abstract*, 1218.
Tanaka, K. and Davis, P. A.: 1988, *J. Geophys. Res.* **93**, 14983.
Thomas, P. C., Veverka, J., Helfenstein, P., Brown, R. H., and Johnson, T. V.: 1987, *J. Geophys. Res.* **92**, 14911.
Thorpe, T. E.: 1976, *Icarus* **27**, 229.
Van Hove, P. L. and Carlotto, M. J.: 1986, *Proc. IGARSS '86*, ESA SP-254, 1011.
Veverka, J., Thomas, P., Johnson, T. V., Matson, D., and Housen, K.: 1986, in J. A. Burns and M. S. Matthews (eds.), *Satellites*, Univ. of Arizona Press, Tucson, 342.
Veverka, J., Thomas, P., Helfenstein, P., Brown, R. H., and Johnson, T. V.: 1987, *J. Geophys. Res.* **92**, 14895.
Wilson, L. and Head, J. W.: 1983, *Nature* **302**, 663.
Wilson, L., Brown, M. A., Parmentier, E. M., and Head, J. W.: 1983, *Lunar Planet. Sci. XIV Abstract*, 849.
Wilson, L., Hampton, J. S., and Balen, H. C.: 1985, *Lunar Planet. Sci. XVI Abstract*, 912.
Wilson, L., Lawson, R., Efford, N. D., and Young, P. C.: 1988, *Proc. IGARSS '88*, ESA SP-284, 429.